CHARGED PION, KAON AND NUCLEON PRODUCTION BY e+e− ANNIHILATION FOR c.m. ENERGIES BETWEEN 3.6 AND 5.2 GeV

DASP Collaboration

R. BRANDELIK, W. BRAUNSCHWEIG, H.-U. MARTYN, H.G. SANDER,
D. SCHMITZ, W. STURM and W. WALLRAFF
I. Physikalisches Institut der RWTH Aachen, Germany

D. CORDS, R. FELST, R. FRIES, E. GADERMANN, H. HULTSCHIG,
P. JOOS, W. KOCH, U. KÖTZ, H. KREHBIEL, D. KREINICK *, H.L.
LYNCH, W.A. MCNEELY **, G. MIKENBERG, K.C. MOFFEIT ***, D. NOTZ,
M. SCHLIWA, A. SHAPIRA †, B.H. WIIK and G. WOLF
Deutsches Elektronen-Synchrotron DESY, Hamburg, Germany

J. LUDWIG ††, K.H. MESS †††, A. PETERSEN, G. POELZ, J. RINGEL,
O. RÖMER, R. RÜSCH, K. SAUERBERG and P. SCHMÜSER
II. Institut für Experimentalphysik der Universität Hamburg, Germany

W. DE BOER, G. BUSCHHORN, W. FUES, Ch. VON GAGERN, G.
GRINDHAMMER, B. GUNDERSON, R. KOTTHAUS, H. LIERL ‡ and
H. OBERLACK
Max-Planck-Institut für Physik und Astrophysik, München, Germany

S. ORITO, T. SUDA, Y. TOTSUKA and S. YAMADA
Lab. of Int. Coll. on Elementary Particle Physics, and Department of Physics, University of Tokyo, Japan

Inclusive production of $\pi^\pm$, $K^\pm$ and $\bar{p}$ has been studied near charm threshold for c.m. energies between 3.6 and 5.2 GeV. Differential and scaling cross sections together with

---

* Now at Cornell University.
** Now at Boeing Computer Services, Seattle, Washington.
*** Now at SLAC.
† On leave from Weizmann Institute, Rehovot, Israel.
†† Now at California Institute of TEchnology.
††† Now at CERN.
‡ Now at University of Dortmund.

particle multiplicities have been determined. By comparing data below and above charm threshold the charm contribution to $\pi^{\pm}$ and $K^{\pm}$ production has been extracted. A comparson has been made between inclusive $\bar{p}$ production and inelastic electron-proton scattering. To study differences between three-gluon annihilation and two-quark production the spectra from J/ψ decay and from non-resonant production at 3.6 GeV have been compared.

1. Introduction

Recent experiments on hadron production by e^+e^- annihilation gave strong evidence for a jet structure of the hadronic final states [1,2]. This evidence together with the observed size of the total e^+e^- cross section support the hypothesis that hadron production proceeds through a primary quark-antiquark pair which in turn fragments into the observed hadrons. Inclusive particle spectra from e^+e^- annihilation can therefore in principle be used for a study of the quark fragmentation functions. These fragmentation functions can be compared with the fragmentation functions deduced from hadron-hadron, charged lepton-nucleon or neutrino-nucleon scattering, which have a different quark composition in the initial state. Compared to the reactions on the nucleon, the e^+e^- data have the advantage that such complications as smearing effects caused by the internal transverse momentum of the initial quark in the nucleon or quark-gluon scattering contributions are absent.

The inclusive spectra from this experiment were taken around the charm threshold. By comparing the data below and above charm threshold it was possible to determine directly the charm quark contribution to hadron production. These measurements may serve as a guide to what happens in general when a new flavour threshold is crossed.

In this paper we present our final results on the inclusive production of charged pions, kaons and nucleons measured for c.m. energies from 3.6 to 5.2 GeV. The experiment was carried out at the DESY e^+e^- storage ring DORIS using the double-arm spectrometer DASP. An analysis based on part of the data as well as a study of inclusive hadron production from J/ψ and ψ' decays can be found in previous publications [3–5].

2. The double-arm spectrometer DASP

A layout of the DASP detector is shown in fig. 1. DASP consists of two identical magnetic spectrometers symmetrically positioned with respect to the interaction point and a non-magnetic detector (solid angle 70% of 4π) in between. Each spectrometer arm has a large H-type magnet with a geometric acceptance from $48°$ to $132°$ in production angle and $\pm 9°$ in azimuth resulting in a solid angle of 0.45 sr for each magnet. The acceptance for charged particles is somewhat smaller than this and depends
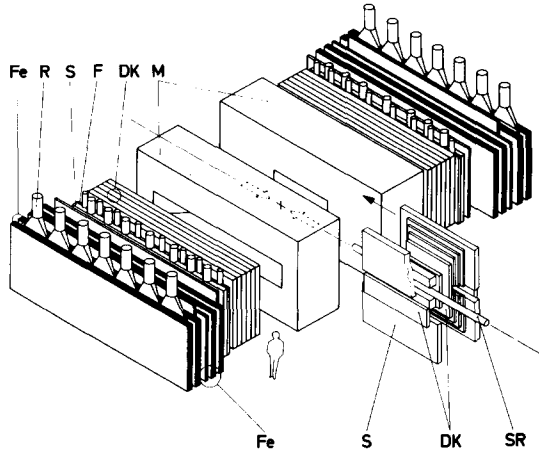
Fig. 1. Schematic view of DASP with the non-magnetic or inner detector moved forward along the beam direction. M: spectrometer magnet. DK: wire spark chamber. F: time-of-flight counters. S: shower counters. R: range counters. Fe: iron absorber.

on the momentum, the field strength, and the last detector plane required in the outer arm. The maximum field strength is 1.1 T, the maximum integrated field length 1.8 Tm.

A charged particle emerging from the interaction point traverses the following detectors before reaching the magnet gap, (see fig. 2) a scintillation counter (S_0) adjacent to the beam pipe, a second scintillation counter (S_0') which starts the time-of-flight measurement, two proportional chambers, each with three signal planes (wire spacing 2 mm), a threshold gas Čerenkov counter, a third scintillation counter (S_M) and a wire spark chamber with magnetostrictive readout (wire spacing 1 mm). Behind the magnet (see fig. 1) follow five wire spark chambers (wire spacing 1 mm), a wall of 31 time-of-flight counters, a wall of 11 shower counters (lead scintillator sandwich with 6.2 radiation lengths), iron plates (total thickness 90 cm) with a wire spark chamber inserted after 40 cm of iron and a wall of a scintillation counters after 60 cm of iron.

The momentum of a charged particle is determined from its trajectory before and behind the magnet. Below some minimum momentum particles are swept out of the spectrometer acceptance. In order to have good acceptance at low momenta the magnets were run at one third and one fifth of the maximum current, leading to a minimum accepted momentum of 0.25 GeV/c and 0.15 GeV/c, respectively. With these settings the r.m.s. momentum resolution for pions of 1 GeV/c momentum was $\Delta p/p \simeq \pm 1\%$ and $\pm 1.4\%$, respectively [6].

Particles are identified by the information from the time-of-flight system, the threshold Čerenkov counter, the shower counter, and the range counter. The r.m.s. time resolution of 0.32 ns and an average flight path of 5 m suffice to separate pions
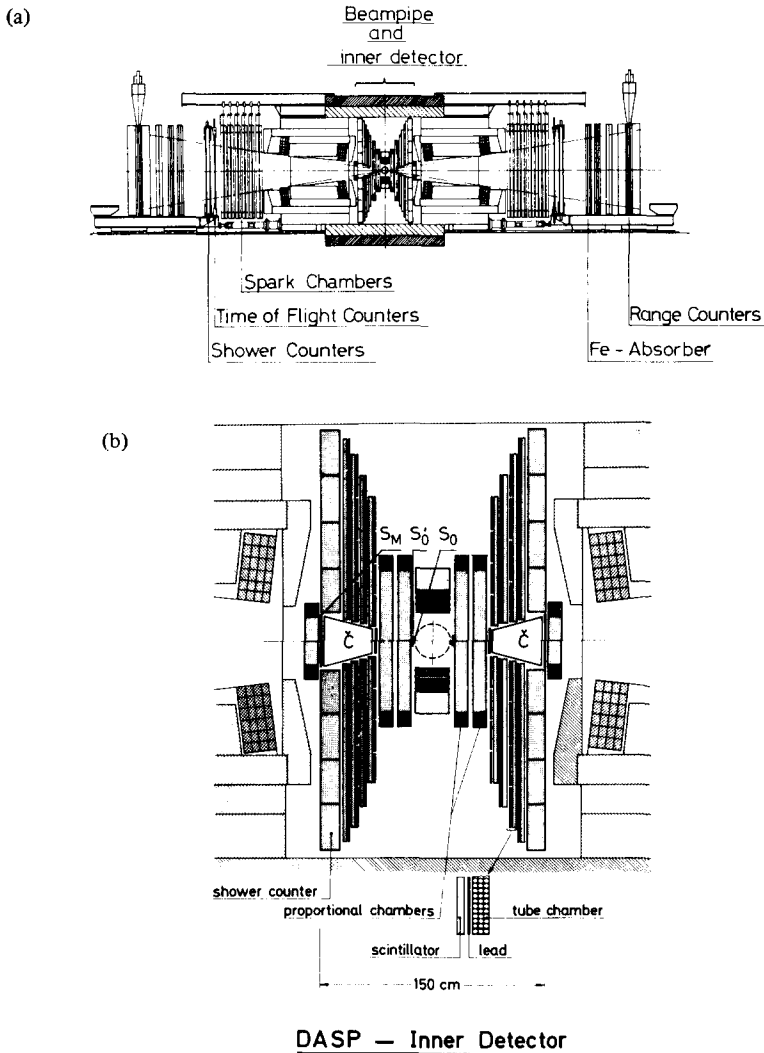
(a)

(b)

DASP — Inner Detector

Fig. 2. (a) View of DASP along the beam direction. (b) The non-magnetic detector viewed along the beam direction.

from kaons up to 1.5 GeV/c, and kaons from protons up to 3 GeV/c [7].

The Čerenkov counter was used to identify electrons. It was filled with freon 114 (n = 1.0014) at atmospheric pressure leading to a threshold of 10 MeV/c for electrons. The thresholds for pions and kaons were 2.7 and 10 GeV/c, respectively, well above the momenta considered here. The efficiency of the Čerenkov counter for

detecting electrons was $(98.8 \pm 0.3)\%$ averaged over the acceptance. The shower counter was also used to identify electrons. For electrons the energy resolution (r.m.s.) of the shower counter was $\sigma \simeq \pm 30\%$ at 1 GeV/c.

The range counter was used to recognize muons. The threshold momentum for muons to reach the counter was roughly 0.9 GeV/c.

The non-magnetic or inner detector located between the two magnets consists of scintillation counters, proportional tube chambers, and shower counters, covering 70% of 4π. It determines the directions of charged particles and photons to within $\pm 2°$ and gives an energy measurement for photons and electrons. The efficiency for detecting photons is 50% for $E_\gamma = 50$ MeV and above 90% for $E_\gamma > 100$ MeV.

3. Data taking and analysing procedure

3.1. Trigger

The data were taken with a genuine inclusive trigger: besides a charged particle in one of the spectrometer arms no other requirement was imposed on the final state. The trigger condition required a coincidence between the scintillation counters, S_0, S_0', S_M, one of the time-of-flight counters (F) and one of the shower counters,

$$T = S_0 \cdot S_0' \cdot S_M \cdot F \cdot S .$$

The minimum momentum to trigger the detector was approximately 0.1 GeV/c for pions, 0.28 GeV/c for kaons and 0.45 GeV/c for protons (antiprotons).

3.2. Luminosity

The luminosity was determined [8] by a measurement of Bhabha scattering using four telescopes centered symmetrically with respect to the interaction point at a

Table 1
Energy intervals and integrated luminosities

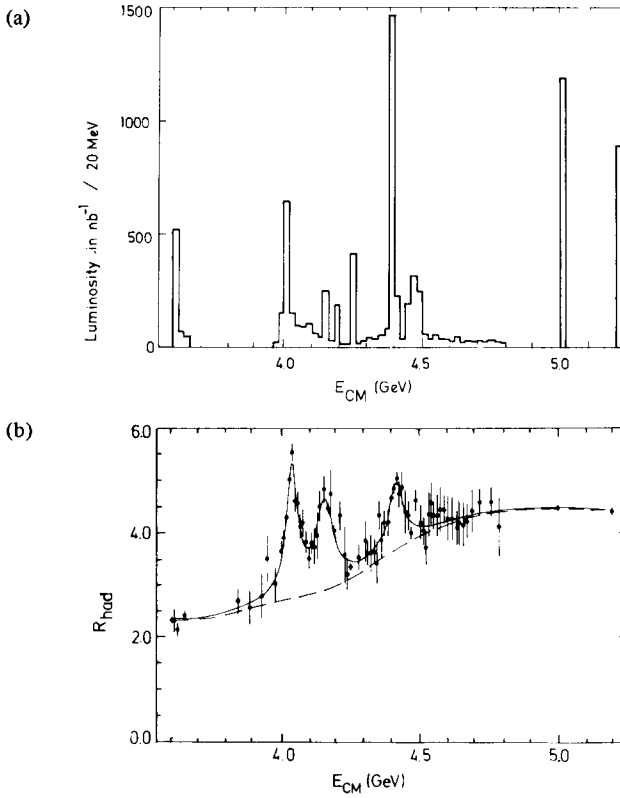| c.m. energy (GeV)	Luminosity (nb^{-1})
3.60–3.67	658
3.98–4.10	1066
4.10–4.24	611
4.24–4.36	533
4.36–4.46	1706
4.46–4.98	1108
5.0	1104
5.2	823

Fig. 3. (a) Integrated luminosity as a function of c.m. energy. (b) The ratio $R = \sigma_{tot}/\sigma_{\mu\mu}$ of the total hadronic cross section to the μ pair cross section. The heavy lepton contribution has been excluded. The full curve shows a fit with three Breit-Wigner resonances plus a parametrized smooth background (dashed curve).

mean scattering angle of 8°. Each telescope was made of two aperture-defining scin-
tillation counters and a shower counter. After applying radiative corrections the
accuracy of the luminosity measurement was typically 5%. Data were taken at c.m.
energies between 3.6 and 5.2 GeV for an integrated luminosity of 7610 nb^{-1}. The
luminosity is not uniformly distributed over this energy region; a large fraction of
the total luminosity is concentrated around a few energy points as can be seen in fig
3a. For comparison fig. 3b shows the total cross section measured in the same exper
iment [9]. The data were grouped into eight different energy intervals listed in
table 1. The first interval is below the charm threshold. The second, third and fifth
intervals are centered around resonance-like structures in the total cross section. The
last points are in a region where R has levelled off.

3.3. Selection criteria *

The interaction volume is 4 cm long and less than 0.1 cm in diameter. In a first step tracks were accepted for which the reconstructed vertex was within ±15 cm of the interaction point measured along the beams (z direction) and within 1 cm measured perpendicular to the beams.

To these tracks the following cuts were applied:

(i) The velocity β measured by time of flight had to be within the range $0.001 < \beta < 1.10$. This cut excludes the majority of the cosmic ray particles.

(ii) Tracks satisfying one of the following requirements were removed as electrons:

(a) The Čerenkov counter was fired. The fraction of pions or kaons that could fire the Čerenkov counter, e.g., *via* a knock-on electron, was measured to be less than 0.2%.

(b) The energy deposited in the shower counter was more than 10 times that for a minimum ionizing particle while the mass inferred from the time of flight was less than the nucleon mass ($M^2(p, \beta) < 0.6$ GeV^2). This leads to a loss of pions or kaons which is small for momenta below 1 GeV/c and which amounts to ~5% for pions or kaons at $1-1.5$ GeV/c.

(c) The momentum was less than 0.25 GeV/c and $M^2(p, \beta) < 0.005$ GeV^2. The loss of hadrons due to this cut is negligible.

(iii) Particles with $M^2(p, \beta) < 0.6$ GeV^2 firing the range counter were identified as muons. The minimum momentum for muons to reach the range counter was 0.9 GeV/c. This cut leads to a loss of pions or kaons due to punch through or decay of $(4 \pm 1)\%$ averaged over momenta between 1 and 1.5 GeV/c.

(iv) Bhabha and muon pairs were further suppressed by discarding events of the following type: there was an additional, collinear track in the opposite spectrometer arm which was identified as an electron or a muon and both tracks had a momentum equal to the beam energy to within 0.1 GeV/c. The number of hadron tracks lost due to this cut is negligible.

(v) An important source of low-energy muons was found in the two-photon process $e^+e^- \rightarrow e^+e^-\mu^+\mu^-$. The kinematics of this process are such that the e^+ and e^- are almost always emitted along the beam direction while the muons are also produced at larger production angles and can reach the spectrometer or the non-magnetic detector. Events of this kind were removed by requiring that for particles of momenta less than 0.6 GeV/c and β consistent with that for a pion at least two more particles (charged ones or photons) were detected in the spectrometer or in the non-magnetic detector. Fig. 4a shows a plot of the computed mass squared $M^2(p, \beta)$ *versus* the vertex position z along the beam for tracks which were removed by the cut and which had momenta less than 0.25 GeV/c.

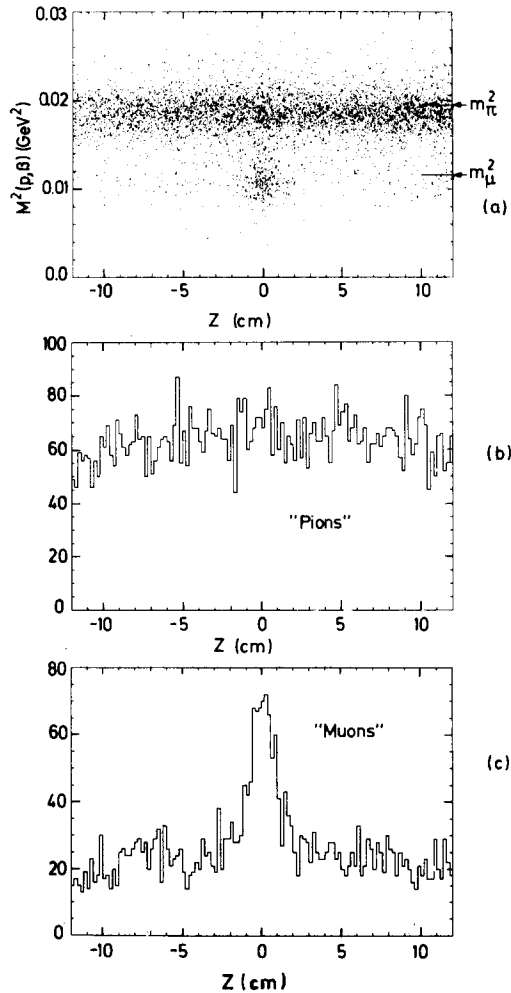* More details of the analysis procedure can be found in ref. [10].

Fig. 4. (a) A plot of the mass squared $M^2(p, \beta)$ determined by momentum and time-of-flight *versus* the position z along the beam line ($z = 0$ marks the interaction point) for particles with momenta less than 250 MeV/c. (b) Projection onto the z axis for $0.016 < M^2(p, \beta) < 0.03$ GeV^2 (pion candidates). (c) Projection onto the z axis for $0 < M^2(p, \beta) < 0.016$ GeV^2 (muon candidates).

The pion mass region is found to be uniformly populated along z (see also projection in fig. 4b). Since no peaking is found near $z = 0$, the pions are produced solely by beam-gas scattering. The multiplicity cut, therefore, does not discard pions originating from beam-beam scattering. In addition to the pion band one observes a pronounced cluster of muons around the interaction point. These muons are due to
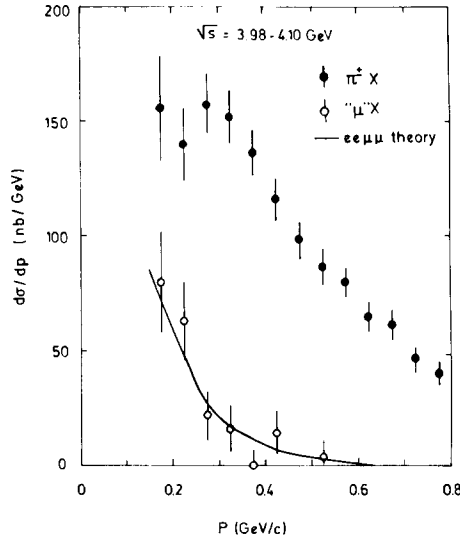
Fig. 5. Differential cross section at c.m. energies 3.98–4.10 GeV for $\pi^{\pm}$ (♦) and muon candidates removed by the multiplicity cut (◊). The solid line shows the inclusive muon cross section from the process $e^{+}e^{-} \to e^{+}e^{-}\mu^{-}\mu^{+}$ calculated by Monte Carlo techniques from theory by incorporating the criteria used in the analysis (e.g., assuming an isotropical production angular distribution to extrapolate to the full solid angle).

beam-beam scattering. The observed rate of muons agrees with that calculated from the two-photon process [11]. For momenta above 0.25 GeV/c the muon/pion separation is no longer perfect. To check that the multiplicity cut which was applied up to 0.6 GeV/c did not remove pions from beam-beam scattering, we computed the number of muons expected from the two-photon process and found it to be in agreement with the number of tracks removed by the multiplicity cut. In fig. 5 the number of muons removed by the multiplicity cut, is removed to the number of accepted pions. The correction for $ee\mu\mu$ events had not been made in our earlier analysis [3].

(vi) No attempt was made to remove muons from charmed particle decay ($e^{+}e^{-} \to c\bar{c} \to \mu X$) or from τ decay ($e^{+}e^{-} \to \tau\bar{\tau} \to \mu X$). From the single-electron events ($e^{+}e^{-} \to eX$) measured in the same experiment [12] and assuming e/μ universality, the fractions of muons from charmed particle and from τ decays were found to be less than 3% and 2%, respectively, of the pion sample.

(vii) The tracks surviving these cuts were classified as pions, kaons or protons (antiprotons) according to their mass-squared values $M^{2}(p, \beta)$ computed from velocity and momentum:

$$M^{2}(p, \beta) = -0.2 - 0.16 \text{ GeV}^{2} : \text{pion} ,$$

$$= 0.16 - 0.4 \text{ GeV}^2: \text{kaon},$$

$$= 0.6 - 2.0 \text{ GeV}^2: \text{proton}.$$

Except for contributions from kaon decay (see below) protons (antiprotons) are uniquely identified by time of flight. Up to 1.2 GeV/c momentum pions and kaons are well separable (see fig. 6). In the momentum interval from 1.2 to 1.5 GeV/c the pion contamination of the kaon signal and the kaon contamination of the pion signal were found to be less than 5%; approximately 20% of the kaons were lost due to the mass cut.

(viii) Since the majority of the protons originated from beam gas interactions, only antiprotons were considered. The proton yield was assumed to be the same as for antiprotons.

The beam gas background was found to be uniformly distributed along the beam axis. To suppress the beam gas background in the remaining track sample a cut was made in the vertex coordinate z measured along the beams. The z position of the interaction point, z_0, was found from Bhabha events measured concurrently in the non-magnetic detector. The z coordinate was required to be within $|z - z_0| < 3.5\sigma$, where σ is the r.m.s. spread of the interaction point distribution; typically $\sigma = 0.9$ cm. The beam gas background, important in the case of low-momentum pions, was extrapolated into the interaction region and was subtracted for each momentum interval. Fig. 7 shows typical z distributions for pions after the aforementioned cuts
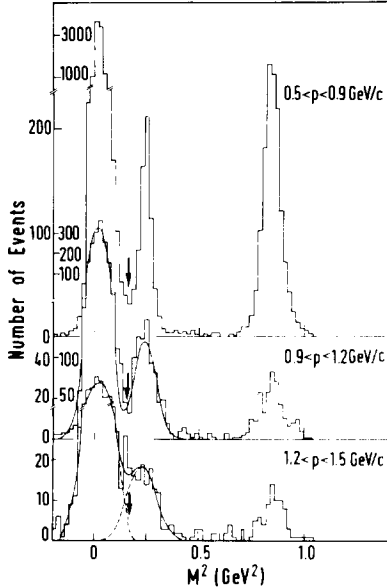

Fig. 6. Histograms of mass squared as computed from particle momentum and time-of-flight for several momentum intervals. The arrows indicate the cut made to separate pions and kaons.
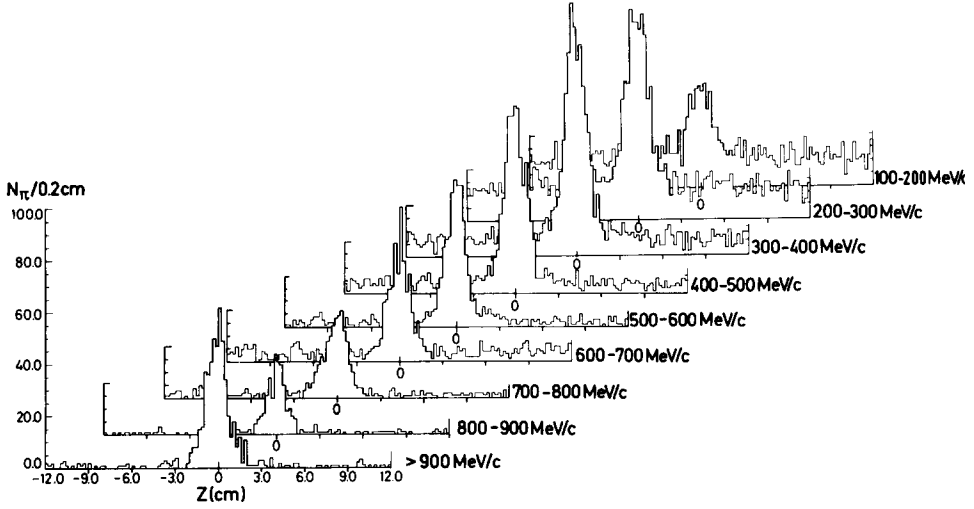
Fig. 7. Vertex distributions of pions measured along the beam direction for different momentum intervals.

were made for various momentum intervals. The fractions of beam gas particles amounted to 25% for momenta $p \simeq 0.2$ GeV/c dropping to 8% at $p = 0.6$ GeV/c and to less than 4% for $p > 0.9$ GeV/c.

(ix) In order to avoid edge effects only tracks within a restricted acceptance of the polar and azimuthal angles were considered. The acceptance typically covered polar angles between $\cos \theta = -0.55$ and 0.55.

(x) The particle momentum was corrected for the energy loss suffered in the material between the interaction point and the exit of the magnet.

3.4. Cross-section determination

Cross sections were computed according to the following expression:

$$d\sigma = \frac{N}{\mathcal{L}} \frac{4\pi}{\Delta\Omega(p)} K \prod_{i=1}^{5} f_i \, dp \,, \qquad (3.1)$$

where N is number of events observed, $\mathcal{L}$ is integrated luminosity, $\Delta\Omega(p)$ is solid angle accepted for a momentum p, K is a correction factor accounting for the corrections discussed above, $f_i, i = 1 \ldots 5$ are further correction factors:

f_1 corrects for nuclear absorption; e.g., for 0.5 GeV/c pions and antiprotons $f_1 = 1.035$ and 1.25, respectively;

f_2 corrects for pion and kaon decay. Between 0.15 and 1.3 GeV/c 42% to 6% of the pions decay before reaching the time-of-flight counter. Of the kaons 71% to 38% decay for momenta between 0.5 and 1.3 GeV/c. However, decaying pions and kaons have a momentum-dependent probability to be accepted by the track-finding

program. A Monte Carlo analysis showed that this probability ranges from 40% to 100% for pions and 5% to 10% for kaons. The effect was included in the correction. Furthermore, a small fraction of the decaying kaons which lead to an accepted track yield a mass-squared value $M^2(p, \beta)$ consistent with that for a proton. The necessary correction factor was determined by a Monte Carlo calculation and led to a reduction of the $\bar{p}$ cross section of $\sim$10% for $\bar{p}$ momenta above 1.2 GeV/c. Below 0.8 GeV/c the correction is negligible.

f_3 corrects for tracks failing the reconstruction, typically $f_3 \simeq 1.03$.

f_4 accounts for track losses due to electronic failure. The value of f_4 is 1.025.

f_5 corrects for radiative effects in the initial state. The energy distribution of the radiated photons was calculated according to Bonneau and Martin [13]. Furthermore, due to the photon emission the c.m. frame is no longer at rest in the laboratory but moves along the beam axis, leading to a change in the acceptance. This effect was also taken into account in the determination of f_5; f_5 was found to be 0.85 at 3.6 GeV, 0.96 at 4.05 GeV and 0.94 above 4.24 GeV. The changing acceptance had only a small effect on the shape of the momentum spectrum. No correction was applied.

The systematic uncertainty in the overall normalization is estimated to be ±15%. The errors shown below do not include this uncertainty; they are purely statistical.

The cross section expression (3.1) assumes an isotropic production angular distribution. Since the beams were unpolarized the general form of the production angular distribution is

$$d\sigma/d\Omega \sim 1 + a \cos^2\theta .$$

We have fitted the angular distribution and determined the coefficient a as a function of particle type, momentum p and c.m. energy. The data for $p < 1.5$ GeV/c are compatible with $a = 0$ but also with $a = 1$. We have assumed $a = 0$ in extrapolating the angular distribution to $\cos \theta = \pm 1$ in order to integrate the differential cross section over $\cos \theta$. For a value of $a = 1$ the cross sections would have to be increased by 24%. The SLAC-LBL collaboration has determined the coefficient a summing over all charged hadrons [14]. Their data indicate for $\sqrt{s} \leqslant 4.8$ GeV, $a \approx 0.2$ for $0.5 < p < 1$ GeV/c and $a \approx 0.5$ for $1 < p < 1.5$ GeV/c. These a values would increase our cross sections by $\approx$5% for values of the scaling variable $x = 2E/\sqrt{s} \leqslant 0.5$ and by $\approx$13% above.

4. General characteristics of charged hadron production

4.1. Kinematics

We start with a brief description of the formalism for inclusive production [15]

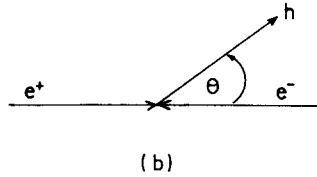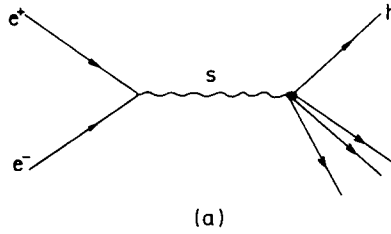$$e^+e^- \rightarrow h^\pm X \tag{4.1}$$

Fig. 8. Diagram for $e^+e^- \to hX$.

depicted in fig. 8. Define

$q = p_+ + p_-$,   four-momentum vector of the virtual photon ,

$q^2 = s$,   square of the c.m. energy ,

$p = (\mathbf{p}, E), p^2 = m^2$,   four-momentum vector of the hadron h ,

θ = production angle of h with respect to the e^+ direction ,

$x = \dfrac{2q \cdot p}{s} = \dfrac{2E}{\sqrt{s}}$,   fractional energy of h ,

$\nu = \dfrac{p \cdot q}{m} = \dfrac{E}{m}\sqrt{s}$,   energy of γ in the h rest system .

Note that $2m\nu/s = x$.

The virtual photon, as seen, e.g., in the rest system of h has two polarization components. As a consequence the differential cross section for h production is described by two independent structure functions when summing over the polarization states of h. Defining these structure functions in close analogy to the corresponding quantities for inelastic lepton-nucleon scattering one writes

$$\frac{d\sigma^2}{dx\,d\Omega}(e^+e^- \to h^\pm X) = \frac{\alpha^2}{s}\,\beta x\{m\overline{W}_1 + \tfrac{1}{4}\beta^2 x\nu\overline{W}_2 \sin^2\theta\} , \qquad (4.2)$$

where $\beta = |\mathbf{p}|/E$ and where the structure functions $m\overline{W}_1$ and $\nu\overline{W}_2$ depend on x and

s. After integrating over the angles one has

$$\frac{d\sigma}{dx} = \frac{4\pi\alpha^2}{s}\beta x \{m\overline{W}_1 + \tfrac{1}{6}\beta^2 x\nu\overline{W}_2\} \ . \tag{4.3}$$

Since the angular distribution was found to be consistent with isotropy we neglect the νW_2 term in eq. (4.3) and obtain

$$\frac{d\sigma}{dx} \simeq \frac{4\pi\alpha^2}{s}\beta x m\overline{W}_1 \ . \tag{4.4}$$

The quantity $(s/\beta) \, d\sigma/dx$ is then proportional to the structure function $\overline{W}_1(x, s)$ [*].

4.2. Experimental results

The cuts discussed previously were satisfied by approximately 13 000 $\pi^\pm$, 890 $K^\pm$ and 130 $\overline{p}$ tracks. This track sample was used for the following analysis.

For the purpose of orientation we begin with the ratio $R = \sigma_{tot}/\sigma_{\mu\mu}$ of the total hadronic cross section to the muon pair cross section shown in fig. 3b. Note that the heavy lepton contribution has been excluded. At 3.6 GeV which is the first c.m. energy analyzed and which is below charm threshold, R is of the order of 2.3. Above charm threshold three resonance-like peaks show up at 4.04, 4.16 and 4.41 GeV. Beyond 4.5 GeV, R seems to have reached its post-charm level with a value of about 4.5.

The relative frequency of pions, kaons and nucleons can be read off from fig. 9 which shows the cross section $d\sigma/dp$ as a function of momentum averaged over c.m. energies from 4 to 5.2 GeV for the sum of π^+ and π^-, K^+ and K^-, and twice the antiproton yield. The dashed curves were obtained from an exponential extrapolation of the invariant cross sections $(E/4\pi p^2) \, d\sigma/dp$ (see below). They indicate the expected momentum dependence at low momenta, where the particles are swept out of the spectrometer due to the magnetic field (pions), are lost by decay (kaons) or suffer too big an energy loss in the material in front of the magnet (antiprotons). At 0.5 GeV/c the $(\pi^+ + \pi^-) : (K^+ + K^-) : 2\overline{p}$ yields are roughly in the ratio 100 : 10 : 1. With increasing momentum the differences between $\pi^\pm$ and $K^\pm$ yields become smaller: at 1.5 GeV/c they are of the same magnitude.

The inclusive cross sections include the contributions from τ pair production,

$$e^+e^- \to \tau\overline{\tau} \to h^\pm X \ .$$

The pion yield from τ production was calculated by Monte Carlo using the decay branching ratios predicted by theory for a τ of 1.8 GeV mass [16]. The pion yield

---

[*] With the *a* coefficients determined by the SLAC-LBL [14] collaboration the contribution of the second term in eq. (4.3) is negative and of the order of 10% for $0.2 < x < 0.4$ (30% for $0.4 < x < 0.6$) relative to the first term.
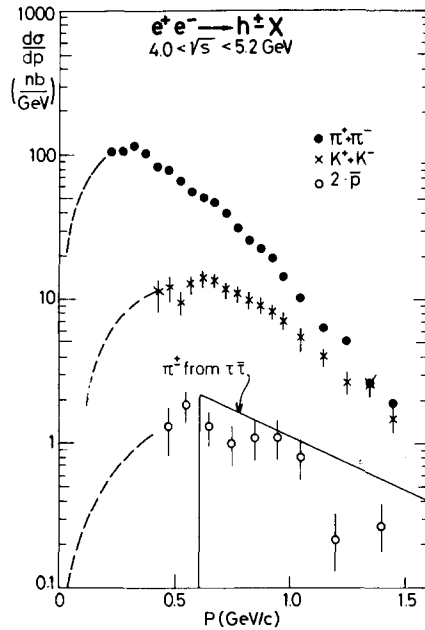
Fig. 9. Differential cross sections $d\sigma/dp$ for the sum of π^+ and π^-, K^+ and K^- and twice the $\bar{p}$ production. The cross sections are averaged over c.m. energies from 4 to 5.2 GeV. The dashed curve shows the expected behaviour at very small momenta obtained from exponential fits to the invariant cross sections. The solid line shows the calculated π^+ contribution from $\tau\bar{\tau}$ production.

is shown by the solid curve in fig. 9. It is suppressed below 0.6 GeV/c because of the selection criteria described above. The τ contribution accounts for ~4% of all pions at $p = 0.6$ GeV/c and ~25% at 1.5 GeV/c. The τ contributions to $K^{\pm}$ and $\bar{p}$ are negligibly small. The data shown below have not been corrected for the contribution from τ production.

Fig. 10 shows the same data plotted in terms of the invariant cross section $E\,d^3\sigma/dp^3 \simeq (E/4\pi p^2)\,d\sigma/dp$. To within 20 or 30% accuracy the $\pi^{\pm}$, $K^{\pm}$ and $2\bar{p}$ cross sections fall on the same curve, which is well-approximated by an exponential,

$$\frac{E}{4\pi p^2}\,\frac{d\sigma}{dp} \sim \exp(-bE) \ .$$

$$E_{cm} = 4\text{--}5.2 \text{ GeV} \ , \qquad b_{\pi} = 5.0 \pm 0.1 \text{ GeV}^{-1} \ ,$$

$$b_K = 4.9 \pm 0.2 \text{ GeV}^{-1} \ , \qquad b_{\bar{p}} = 5.4 \pm 0.5 \text{ GeV}^{-1} \ .$$

Inclusive spectra in hadronic collisions behave in a similar manner when plotted as a function of the transverse energy $E_T = \sqrt{m^2 + p_T^2}$ instead of the energy E (see, e.g., ref. [17]).
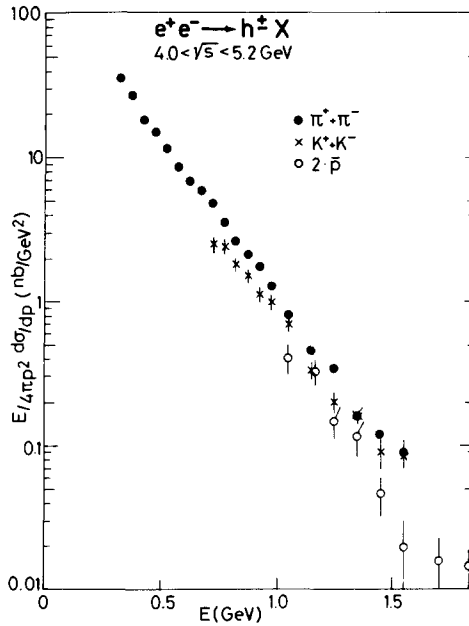
Fig. 10. Invariant cross sections $(E/4\pi p^2)\, d\sigma/dp$ as a function of particle energy E. Same data as in fig. 9.

5. *s* dependence and charm contribution

Within the energy region investigated (3.6–5.2 GeV) lies the charm threshold. To allow for a detailed study of the new flavour contribution the data were grouped into eight c.m. energy intervals as listed in table 1.

5.1. Momentum distributions

We start with the momentum distributions. They are collected in fig. 11 in terms of $d\sigma/dp$ for the eight c.m. energy intervals. For convenience the cross sections are also tabulated in table 2. A significant rise in the pion and kaon yields is observed between $\sqrt{s}$ = 3.6 and 4 GeV. This rise is almost exclusively due to charmed particle production. Fig. 12 shows the same data plotted in terms of the invariant cross sections, $(E/4\pi p^2)\, d\sigma/dp$. As expected from the combined data shown in fig. 10, a single exponential gives a good fit to the data,

$$\frac{E}{4\pi p^2}\frac{d\sigma}{dp} = a\,\exp\left[-b(E - E_0)\right]\,, \tag{5.1}$$

where E_0 was chosen to be 1 GeV.

$$e^+ e^- \longrightarrow h^\pm X$$

- $\pi^+ + \pi^-$
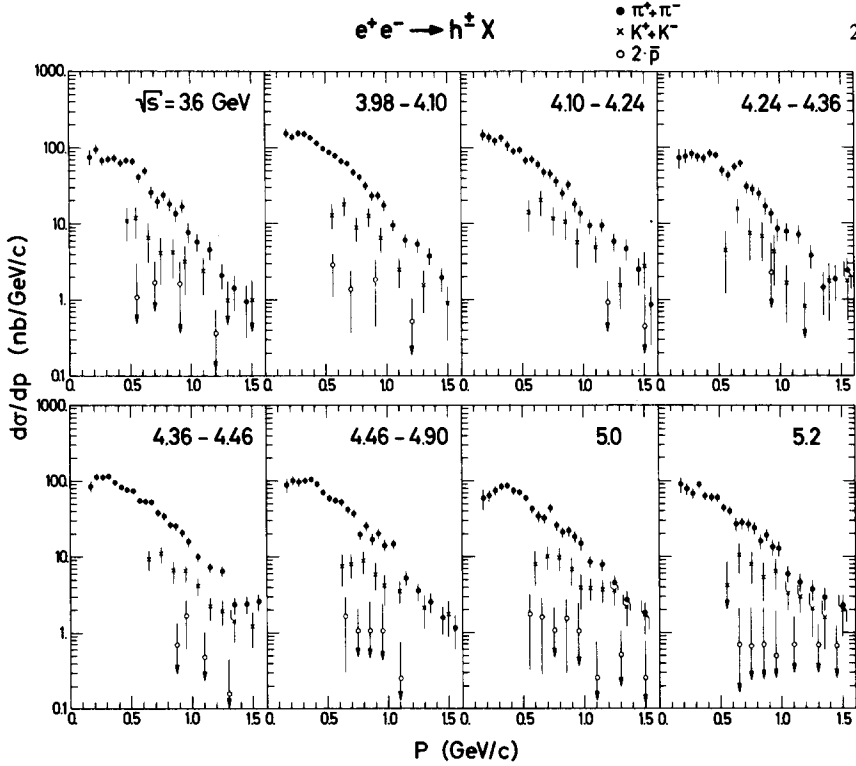- $\times\ K^+ + K^-$
- $\circ\ 2 \cdot \bar{p}$

Fig. 11. Differential cross sections $d\sigma/dp$ for the sum of π^+, and π^-, K^+ and K^- and twice the $\bar{p}$ production for eight different c.m. energies.
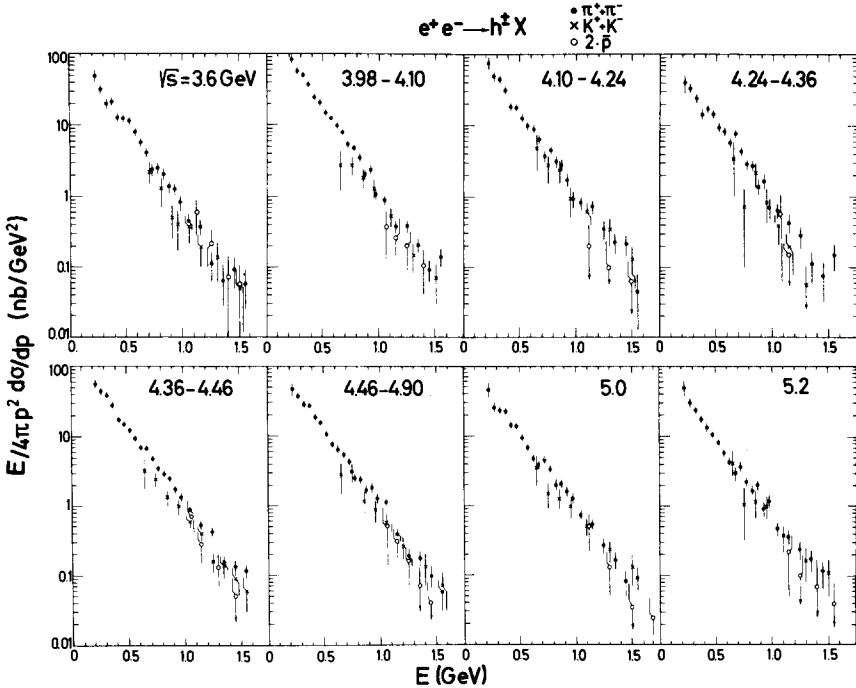

Fig. 12. Invariant cross sections $(E/4\pi p^2)\,d\sigma/dp$ as a function of particle energy. Same data as in

Table 2
Differential cross sections $d\sigma/dp$ in (mb/(GeV/c)) for the sum of $\pi^+ + \pi^-$, $K^+ + K^-$ and $2\bar{p}$ production for different c.m. energies $\sqrt{s}$; the errors given are purely statistical

(a) $\pi^+ + \pi^-$

Momentum p (GeV/c)	$\sqrt{s}$ (GeV) 3.60–3.67	3.98–4.10	4.10–4.24	4.24–4.36	4.36–4.46	4.46–4.98	5.0	5.2
0.15–0.20	77.09 ± 18.22	156.40 ± 22.56	148.08 ± 27.90	75.47 ± 22.85	88.86 ± 14.88	87.30 ± 18.82	56.81 ± 18.00	88.24 ± 21.74
0.20–0.25	97.51 ± 14.46	139.74 ± 15.79	136.12 ± 19.72	76.40 ± 15.05	117.14 ± 10.86	99.75 ± 12.37	62.20 ± 11.23	76.63 ± 13.43
0.25–0.30	67.81 ± 10.55	158.31 ± 13.30	120.35 ± 16.17	84.33 ± 13.38	114.88 ± 9.53	94.48 ± 11.23	71.94 ± 9.76	66.06 ± 10.61
0.30–0.35	71.07 ± 9.42	152.36 ± 11.53	133.42 ± 14.58	75.07 ± 11.14	118.33 ± 8.34	99.05 ± 9.98	80.16 ± 8.85	86.40 ± 10.58
0.35–0.40	73.24 ± 9.02	136.15 ± 10.12	109.53 ± 12.45	73.00 ± 10.32	97.23 ± 6.98	102.10 ± 8.93	83.73 ± 7.96	61.65 ± 8.49
0.40–0.45	62.73 ± 7.67	116.18 ± 8.72	88.89 ± 10.57	84.61 ± 10.44	84.81 ± 6.14	88.62 ± 7.92	70.51 ± 7.20	59.53 ± 7.48
0.45–0.50	68.42 ± 7.85	98.06 ± 7.79	92.25 ± 10.26	78.89 ± 9.65	78.34 ± 5.70	69.35 ± 6.78	67.72 ± 6.42	58.33 ± 7.17
0.50–0.55	67.05 ± 7.55	86.69 ± 7.21	66.62 ± 8.57	49.09 ± 7.54	75.12 ± 5.26	57.65 ± 6.05	57.49 ± 5.83	43.42 ± 5.84
0.55–0.60	40.30 ± 5.82	79.71 ± 6.83	69.70 ± 8.61	42.72 ± 6.98	55.30 ± 4.60	54.64 ± 5.53	41.78 ± 4.95	39.18 ± 5.57
0.60–0.65	49.80 ± 6.54	65.40 ± 6.52	58.50 ± 8.13	55.01 ± 7.73	54.58 ± 4.71	50.96 ± 5.87	33.28 ± 5.16	26.47 ± 5.48
0.65–0.70	25.80 ± 4.65	61.85 ± 5.91	46.66 ± 6.86	61.69 ± 8.09	53.59 ± 4.42	41.06 ± 5.04	31.45 ± 4.43	27.39 ± 4.98
0.70–0.75	19.30 ± 3.91	46.72 ± 4.98	44.72 ± 6.58	30.07 ± 5.62	38.70 ± 3.70	36.54 ± 4.46	42.60 ± 4.84	26.59 ± 4.64
0.75–0.80	23.63 ± 4.12	40.63 ± 4.66	35.68 ± 5.79	28.14 ± 5.37	34.94 ± 3.42	19.04 ± 3.14	24.99 ± 3.64	28.65 ± 4.35
0.80–0.85	18.00 ± 3.64	31.16 ± 4.07	24.39 ± 4.70	24.43 ± 4.89	26.93 ± 2.99	24.87 ± 3.61	20.49 ± 3.31	15.66 ± 3.50
0.85–0.90	13.46 ± 3.15	22.97 ± 3.56	32.12 ± 5.37	16.76 ± 4.07	25.04 ± 2.84	16.81 ± 2.91	21.41 ± 3.32	18.96 ± 3.58
0.90–0.95	16.89 ± 3.61	23.05 ± 3.45	17.84 ± 4.05	13.23 ± 3.69	20.86 ± 2.57	19.75 ± 3.11	17.62 ± 2.99	13.17 ± 3.17
0.95–1.00	7.62 ± 2.37	17.01 ± 3.00	13.37 ± 3.50	8.46 ± 2.91	16.09 ± 2.30	13.90 ± 2.68	14.45 ± 2.70	12.76 ± 2.96
1.00–1.10	5.76 ± 1.48	9.49 ± 1.56	9.12 ± 2.03	7.83 ± 2.01	10.13 ± 1.27	14.30 ± 1.86	8.33 ± 1.44	5.88 ± 1.45
1.10–1.20	4.56 ± 1.26	6.00 ± 1.25	9.46 ± 2.05	7.15 ± 1.93	7.32 ± 1.08	5.18 ± 1.13	7.54 ± 1.34	4.57 ± 1.29
1.20–1.30	2.09 ± 0.85	5.30 ± 1.13	5.79 ± 1.59	3.80 ± 1.34	6.61 ± 1.01	3.46 ± 0.92	4.44 ± 1.03	3.67 ± 1.12
1.30–1.40	1.40 ± 0.70	3.71 ± 0.97	4.64 ± 1.40	1.43 ± 0.82	2.36 ± 0.60	2.52 ± 0.76	2.67 ± 0.79	2.89 ± 0.98
1.40–1.50	0.93 ± 0.62	1.93 ± 0.68	2.53 ± 1.03	1.89 ± 0.95	2.40 ± 0.60	1.53 ± 0.61		

(b) $K^+ + K^-$

Momentum p (GeV/c)	$\sqrt{s}$ (GeV) 3.60–3.67	Momentum p (GeV/c)	$\sqrt{s}$ (GeV) 3.98–4.10	Momentum p (GeV/c)	$\sqrt{s}$ (GeV) 4.10–4.24	Momentum p (GeV/c)	$\sqrt{s}$ (GeV) 4.24–4.36
0.45–0.50	10.89 ± 5.49	0.50–0.60	13.86 ± 4.04	0.50–0.60	13.93 ± 6.23	0.50–0.60	4.40 ± 3.60
0.50–0.60	11.34 ± 5.09	0.60–0.70	17.40 ± 4.80	0.60–0.70	20.27 ± 6.92	0.60–0.70	15.70 ± 6.17
0.60–0.70	6.49 ± 3.48	0.70–0.80	8.67 ± 3.21	0.70–0.80	11.41 ± 4.50	0.70–0.80	7.60 ± 4.03
0.70–0.80	4.00 ± 2.53	0.80–0.90	12.69 ± 3.40	0.80–0.90	10.17 ± 4.14	0.80–0.90	6.71 ± 3.58

Momentum p (GeV/c)	√s (GeV) 4.36-4.46	Momentum p (GeV/c)	√s (GeV) 4.46-4.98	Momentum p (GeV/c)	√s (GeV) 5.0	Momentum p (GeV/c)	√s (GeV) 5.2
0.80-0.90	4.17 ± 2.41	0.90-1.00	6.39 ± 2.51	0.90-1.00	5.57 ± 2.98	0.90-1.00	4.29 ± 2.79
0.90-1.00	3.12 ± 1.98	1.00-1.20	2.42 ± 1.02	1.00-1.10	4.84 ± 1.81	1.00-1.10	1.64 ± 1.16
1.00-1.20	2.35 ± 1.17	1.20-1.40	1.59 ± 0.94	1.20-1.40	1.55 ± 1.05	1.10-1.30	1.64 ± 1.16
1.20-1.40	0.97 ± 0.79	1.40-1.60	0.89 ± 0.56	1.40-1.60	0.45 ± 0.91	1.30-1.50	1.75 ± 1.25
1.40-1.60	0.98 ± 0.80					1.50-1.60	1.78 ± 1.26

Momentum p (GeV/c)	√s (GeV) 4.36-4.46	Momentum p (GeV/c)	√s (GeV) 4.46-4.98	Momentum p (GeV/c)	√s (GeV) 5.0	Momentum p (GeV/c)	√s (GeV) 5.2
0.60-0.70	9.55 ± 2.77	0.60-0.65	8.51 ± 3.23	0.55-0.65	7.72 ± 3.90	0.50-0.60	4.11 ± 4.28
0.70-0.80	11.22 ± 2.76	0.65-0.75	7.88 ± 2.88	0.65-0.75	9.83 ± 3.32	0.60-0.70	10.36 ± 4.42
0.80-0.90	6.92 ± 2.04	0.75-0.85	8.72 ± 2.90	0.75-0.85	9.41 ± 3.15	0.70-0.80	7.77 ± 3.42
0.90-1.00	6.62 ± 1.91	0.85-0.95	5.76 ± 2.26	0.85-0.95	6.57 ± 2.54	0.80-0.90	5.36 ± 2.81
1.00-1.10	4.35 ± 1.06	0.95-1.00	4.04 ± 1.81	0.95-1.00	3.79 ± 1.84	0.90-1.00	6.34 ± 2.78
1.10-1.20	2.22 ± 0.74	1.00-1.20	3.49 ± 1.16	1.00-1.10	3.76 ± 1.23	1.00-1.10	3.24 ± 1.32
1.20-1.40	1.98 ± 0.75	1.20-1.40	2.14 ± 0.96	1.10-1.20	3.55 ± 1.17	1.10-1.20	2.95 ± 1.20
1.30-1.40	1.41 ± 0.63	1.40-1.60	1.71 ± 0.86	1.20-1.30	3.40 ± 1.20	1.20-1.30	2.03 ± 1.18
1.40-1.60	1.26 ± 0.60			1.30-1.40	2.10 ± 0.94	1.30-1.40	1.59 ± 1.02

(c) 2p̄

Momentum p (GeV/c)	√s (GeV) 3.60-3.67	Momentum p (GeV/c)	√s (GeV) 3.98-4.10	Momentum p (GeV/c)	√s (GeV) 4.10-4.24	Momentum p (GeV/c)	√s (GeV) 4.24-4.36
0.50-0.60	1.01 ± 1.01	0.50-0.60	2.97 ± 1.87	1.10-1.30	0.92 ± 0.92	0.90-0.95	2.25 ± 2.25
0.60-0.80	1.63 ± 1.63	0.60-0.75	1.42 ± 1.06				
0.80-1.00	1.56 ± 1.56	0.75-1.00	1.84 ± 1.37				
1.00-1.40	0.36 ± 0.36	1.00-1.40	0.52 ± 0.52				

Momentum p (GeV/c)	√s (GeV) 4.36-4.46	Momentum p (GeV/c)	√s (GeV) 4.46-4.98	Momentum p (GeV/c)	√s (GeV) 5.10	Momentum p (GeV/c)	√s (GeV) 5.2
0.85 - 0.90	0.70 ± 0.70	0.60-0.70	1.61 ± 1.32	0.50-0.60	1.17 ± 1.39	0.60-0.70	0.69 ± 1.38
0.90 - 1.00	1.70 ± 1.08	0.70-0.80	1.04 ± 1.04	0.60-0.70	1.57 ± 1.29	0.70-0.80	0.68 ± 1.37
1.00-1.20	0.50 ± 0.50	0.80-0.90	1.05 ± 1.50	0.70-0.80	1.02 ± 1.02	0.80-0.90	0.69 ± 1.39
1.20-1.40	0.16 ± 0.32	0.90-1.00	1.10 ± 1.42	0.80-0.90	1.51 ± 1.22	0.90-1.00	0.68 ± 1.36
		1.00-1.20	0.26 ± 0.50	0.90-10.0	1.00 ± 1.42	1.00-1.20	0.67 ± 0.95
				1.00-0.49	0.25 ± 0.49	1.20-1.40	0.67 ± 0.67
						1.40-1.50	0.66 ± 0.66

Table 3
Intercept and slope values from fit $(E/4\pi p^2)\,\mathrm{d}\sigma/\mathrm{d}p = a\,\exp[-b(E - E_0)]$, $E_0 = 1$ GeV; a in (nb GeV^{-2}), b in (GeV^{-1})

$\sqrt{s}$ (GeV)	$\pi^+ + \pi^-$		$K^+ + K^-$	
	a	b	a	b
3.60–3.67	0.70 ± 0.05	5.34 ± 0.14	0.42 ± 0.07	4.6 ± 0.9
3.98–4.10	1.22 ± 0.06	5.37 ± 0.09	0.77 ± 0.11	4.8 ± 0.5
4.10–4.24	1.18 ± 0.07	5.11 ± 0.13	0.99 ± 0.15	4.2 ± 0.7
4.24–4.36	0.93 ± 0.06	4.91 ± 0.14	0.39 ± 0.09	5.0 ± 0.9
4.36–4.46	1.20 ± 0.04	4.94 ± 0.08	0.70 ± 0.07	4.7 ± 0.5
4.46–4.98	0.99 ± 0.05	5.07 ± 0.10	0.70 ± 0.09	4.4 ± 0.4
5.0	0.99 ± 0.05	4.72 ± 0.11	0.72 ± 0.10	3.7 ± 0.4
5.2	0.73 ± 0.06	5.08 ± 0.17	0.61 ± 0.11	3.8 ± 0.6
$\sqrt{s}$ (GeV)	$2\bar{p}$:			
4.0–5.2	0.63 ± 0.10	5.5 ± 0.6		

The values of the coefficients a and b are listed in table 3; b is shown also in fig. 13. No significant change in slope is found when crossing the charm threshold. The pion slope within errors is constant over the full energy range; the kaon slope appears to fall slightly with energy.

5.2. Particle multiplicities

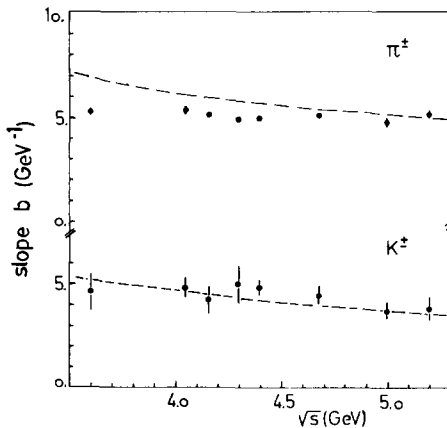From the measured momentum distributions the average numbers of charged

Fig. 13. The slope b for $\pi^\pm$ and $K^\pm$ production resulting from fits of the invariant cross sections $(E/4\pi p^2)\,\mathrm{d}\sigma/\mathrm{d}p \propto \exp(-bE)$.
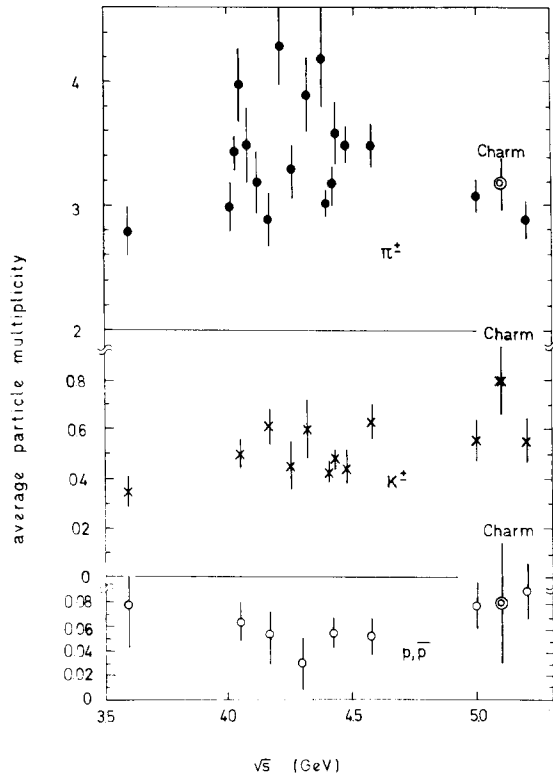
Fig. 14. Average multiplicity of charged pions, kaons and nucleons per event as a function of c.m. energy. The points labeled "charm" give the multiplicities for charmed events alone (see text).

pions, kaons and nucleons have been calculated, e.g.,

$$\langle n_{\pi^{\pm}} \rangle = \frac{\int_{0}^{p_{max}} \frac{d\sigma}{dp}(e^{+}e^{-} \to \pi^{\pm}X)\, dp}{\sigma_{tot}}.$$

The extrapolation of $d\sigma/dp$ to zero momentum has been done using the exponential fits described by eq. (5.1). For σ_{tot} the data obtained in the same experiment [9] have been used. The fraction of the cross section determined by extrapolation amounted to 10% for the majority of the pion data, to 20% for kaons and to 30% for antiprotons. The particle multiplicities are shown in fig. 14 as a function of the c.m. energy. The errors given are purely statistical. The systematic errors of the inte grated inclusive cross sections and of σ_{tot} add a further uncertainty of 20–25% of which ~15% are due to normalization. Above charm threshold on the average 3–4 $\pi^{\pm}$, 0.5–0.6 $K^{\pm}$ and 0.05–0.08 p and $\bar{p}$ are produced per event.

5.3. Scaling cross sections

In general the structure functions $\overline{W}_1$ and $\nu\overline{W}_2$ depend on two variables, e.g., x and s. If scale invariance is fulfilled $\overline{W}_1$ and $\nu\overline{W}_2$ are functions of x alone and the cross section $(s/\beta)\,d\sigma/dx$, is almost the same for all values of s (see eq. (4.4)).

In fig. 15 the scaling cross sections $(s/\beta)\,d\sigma/dx$ for $\pi^\pm$, $K^\pm$ and $2\overline{p}$ production have been plotted as a function of x in the eight energy intervals. The scaling cross sections are also listed in table 4. Most spectacular is the similarity between the three types of particles. Within a factor of two their cross sections seem to fall on a common curve decreasing exponentially for $x \gtrsim 0.2$. No peculiarities are observed when comparing the shapes of the cross sections measured at the resonances (second, third and fifth interval) and outside.

In order to test the pion data for scaling we compare in fig. 16 the π cross sections outside the resonance region at energies of $\sqrt{s} = 3.6$ and 5.2 GeV. Below $x = 0.25$ the cross section rises by a factor of 1.5 to 2 between $\sqrt{s} = 3.6$ and 5.2 GeV. At higher x values the two cross-section sets agree within errors. This shows that the
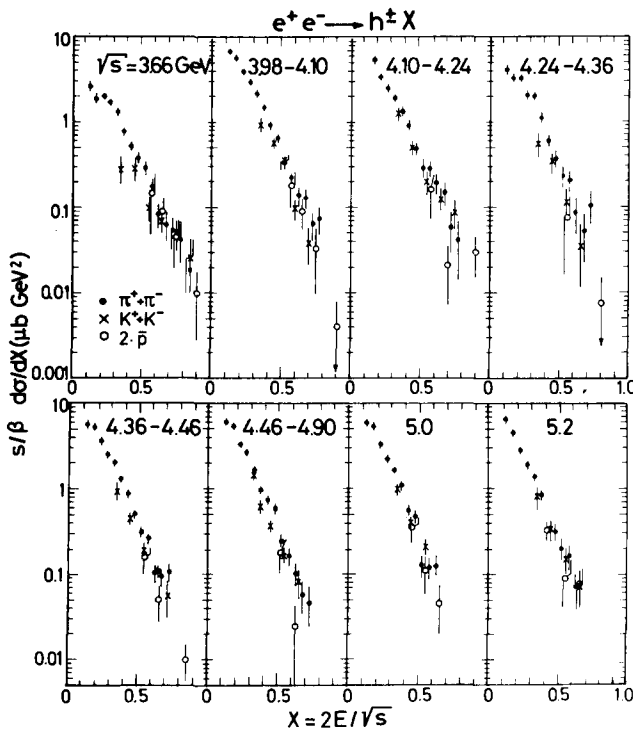

Fig. 15. Scaling cross sections $(s/\beta)\,d\sigma/dx$ as a function of x. Same data as in fig. 11.

Table 4

Scaling cross sections $(s/\beta)\, d\sigma/dx$ in nb · GeV^2 for the sum of $\pi^+ + \pi^-$, $K^+ + K^-$ and $2\bar{p}$ production for different c.m. energies $\sqrt{s}$; the errors given are purely statistical

(a) $\pi^+ + \pi^-$

$x = 2E/\sqrt{s}$	$\sqrt{s}$ (GeV) 3.60–3.67	3.98–4.10	4.10–4.24	4.24–4.36
0.10–0.15	2704.4 ± 412.6	7042.5 ± 603.7		4048.8 ± 538.1
0.15–0.20	1943.4 ± 230.5	5968.9 ± 312.2	5623.5 ± 409.5	3343.6 ± 328.6
0.20–0.25	2023.7 ± 174.6	4103.0 ± 215.6	3486.8 ± 277.1	3276.9 ± 277.8
0.25–0.30	1716.2 ± 145.4	3063.3 ± 175.4	2567.2 ± 224.1	2088.2 ± 209.8
0.30–0.35	1329.2 ± 122.6	2243.6 ± 150.4	1926.4 ± 189.7	2002.9 ± 199.8
0.35–0.40	793.4 ± 93.2	1523.3 ± 116.7	1367.5 ± 152.3	1127.6 ± 145.1
0.40–0.45	525.2 ± 71.9	941.3 ± 91.3	943.6 ± 122.1	606.5 ± 105.9
0.45–0.50	387.1 ± 61.5	667.1 ± 75.6	490.0 ± 88.7	377.2 ± 84.0
0.50–0.55	294.6 ± 54.6	335.4 ± 52.9	296.2 ± 69.4	231.9 ± 66.5
0.55–0.60	170.6 ± 41.3	221.1 ± 43.2	287.8 ± 66.5	204.5 ± 60.4
0.60–0.65	83.0 ± 27.7	141.3 ± 33.3	192.7 ± 53.5	87.6 ± 39.2
0.65–0.70	64.1 ± 24.2	130.1 ± 32.9	147.9 ± 46.8	52.1 ± 30.1
0.70–0.75	55.0 ± 22.4	63.8 ± 22.6	58.1 ± 29.0	105.9 ± 43.3
0.75–0.80	42.7 ± 20.7	73.3 ± 24.4	41.4 ± 27.6	
0.80–0.90	18.6 ± 9.3	42.1 ± 10.5		

$x = 2E/\sqrt{s}$	$\sqrt{s}$ (GeV) 4.36–4.46	4.46–4.98	5.0	5.2
0.10–0.15	5609.1 ± 346.3	5664.8 ± 461.9	6017.1 ± 481.5	6554.9 ± 566.5
0.15–0.20	5234.0 ± 242.6	5361.6 ± 314.7	5458.2 ± 322.9	4598.0 ± 358.3
0.20–0.25	3648.2 ± 173.3	3341.5 ± 216.9	3341.2 ± 229.4	2827.0 ± 259.7
0.25–0.30	2589.9 ± 141.9	2606.1 ± 184.9	2277.5 ± 197.6	1907.3 ± 214.7
0.30–0.35	2037.1 ± 120.6	1619.3 ± 138.5	1679.4 ± 151.2	1347.3 ± 168.3

Table 4 (continued)

(continuation)

x = 2E/√s				
0.35–0.40	1338.1 ± 93.5	950.8 ± 101.4	1101.8 ± 119.3	835.8 ± 128.2
0.40–0.45	878.6 ± 74.2	731.0 ± 87.6	560.8 ± 83.9	325.0 ± 83.0
0.45–0.50	500.7 ± 56.1	572.9 ± 75.7	468.9 ± 73.4	317.2 ± 75.3
0.50–0.55	319.5 ± 44.9	237.7 ± 49.6	127.8 ± 40.1	202.8 ± 60.7
0.55–0.60	261.1 ± 39.4	158.7 ± 38.5	119.7 ± 38.4	166.4 ± 56.2
0.60–0.65	103.9 ± 25.0	100.1 ± 31.3	119.1 ± 38.3	69.9 ± 34.9
0.65–0.70	93.4 ± 23.3	55.3 ± 23.7		
0.70–0.75	107.7 ± 26.1	46.5 ± 23.3		
0.75–0.80				
0.80–0.90				
0.90–1.00				

(b) K⁺ + K⁻

x = 2E/√s	√s (GeV) 3.60–3.67	x = 2E/√s	√s (GeV) 3.98–4.10	x = 2E/√s	√s (GeV) 4.10–4.24	x = 2E/√s	√s (GeV) 4.24–4.36
0.30–0.40	270 ± 100	0.30–0.40	954 ± 244	0.30–0.40	1248 ± 355	0.30–0.40	570 ± 190
0.40–0.50	296 ± 62	0.40–0.50	580 ± 113	0.40–0.50	538 ± 137	0.40–0.50	331 ± 86
0.50–0.55	104 ± 30	0.50–0.60	344 ± 79	0.50–0.60	201 ± 65	0.50–0.60	125 ± 52
0.55–0.65	72 ± 24	0.60–0.70	96 ± 40	0.60–0.70	128 ± 38	0.60–0.70	36 ± 25
0.65–0.75	51 ± 22	0.70–0.80	41 ± 26	0.70–0.80	92 ± 38		
0.75–0.85	25 ± 18	0.80–0.90					

x = 2E/√s	√s (GeV) 4.36–4.46	x = 2E/√s	√s (GeV) 4.46–4.98	x = 2E/√s	√s (GeV) 5.0	x = 2E/√s	√s (GeV) 5.2
0.30–0.40	936 ± 215	0.30–0.35	1457 ± 248	0.30–0.40	947 ± 137	0.30–0.40	820 ± 366
0.40–0.50	454 ± 79	0.35–0.40	628 ± 139	0.40–0.50	411 ± 76	0.40–0.50	349 ± 69
0.50–0.60	195 ± 37	0.40–0.50	370 ± 68	0.50–0.60	225 ± 39	0.50–0.60	146 ± 54
0.60–0.70	105 ± 22	0.50–0.60	170 ± 65			0.60–0.70	76 ± 41
0.70–0.75	55 ± 25	0.60–0.70	81 ± 34				

Table 4 (continued)
(c) $2\bar{p}$

$x = 2E/\sqrt{s}$	$\sqrt{s}$ (GeV) 3.60–3.67	$x = 2E/\sqrt{s}$	$\sqrt{s}$ (GeV) 3.98–4.10	$x = 2E/\sqrt{s}$	$\sqrt{s}$ (GeV) 4.10–4.24	$x = 2E/\sqrt{s}$	$\sqrt{s}$ (GeV) 4.24–4.36
0.55–0.60	145 ± 55	0.55–0.60	182 ± 84	0.55–0.60	164 ± 95	0.50–0.60	74 ± 59
0.60–0.70	86 ± 34	0.60–0.70	91 ± 94	0.60–0.80	21 ± 14		
0.70–0.80	45 ± 28	0.70–0.80	33 ± 27	0.80–1.00	30 ± 15		
0.80–1.00	10 ± 7	0.80–1.00	4 ± 4				

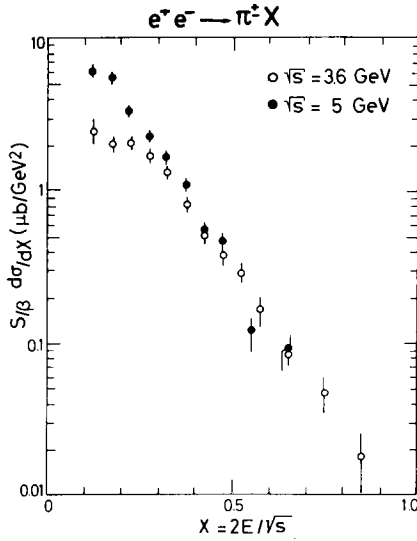| $x = 2E/\sqrt{s}$	$\sqrt{s}$ (GeV) 4.36–4.46	$x = 2E/\sqrt{s}$	$\sqrt{s}$ (GeV) 4.46–4.98	$x = 2E/\sqrt{s}$	$\sqrt{s}$ (GeV) 5.0	$x = 2E/\sqrt{s}$	$\sqrt{s}$ (GeV) 5.2
0.50–0.60	163 ± 61	0.50–0.60	176 ± 79	0.40–0.50	332 ± 101	0.50–0.50	92 ± 51
0.60–0.70	54 ± 22	0.60–0.65	25 ± 19	0.50–0.60	109 ± 52	0.60–0.70	80 ± 45
0.70–0.75	10 ± 5			0.60–0.70	46 ± 27		

Fig. 16. Comparison of the scaling cross sections $(s/\beta)\, d\sigma/dx$ *versus* x for $\pi^{\pm}$ at $s = 13$ and 27 GeV^2.
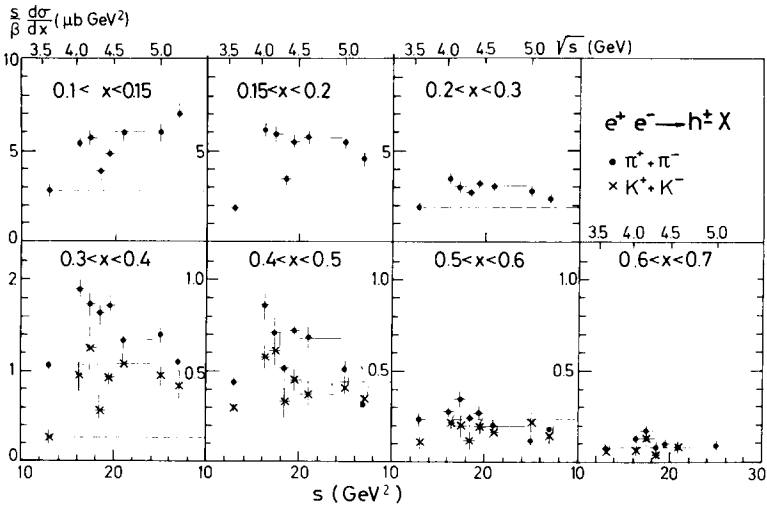

Fig. 17. The scaling cross sections $(s/\beta)\, d\sigma/dx$ *versus* s for fixed x intervals for $\pi^{\pm}$ and K$^{\pm}$ production.

rise of R from a value of 2.3 at $\sqrt{s}$ = 3.6 GeV to 4.5 above $\sqrt{s}$ = 5 GeV is associated with *low x* pions.

Fig. 17 shows the $\pi^\pm$ and $K^\pm$ data plotted as a function of s for fixed x. Both cross sections for $x < 0.5$ rise by a factor of two to three when crossing the charm threshold near $\sqrt{s}$ = 4 GeV. In the pion case for $x > 0.2$ this added contribution disappears above the resonance region. For $x > 0.3$ the scaling cross section at $\sqrt{s}$ = 5.2 GeV has reached its precharm level measured at $\sqrt{s}$ = 3.6 GeV. For kaons this occurs at slightly higher x values, $x \approx 0.4$. We may therefore expect that at much higher energies ($\sqrt{s} \gg 5$ GeV) the charm contribution is confined to x values less than 0.3.

5.4. Charm contribution to $\pi^\pm$ and $K^\pm$ production

We have determined the charm contribution to charged pion and kaon production as the difference in the cross sections for c.m. energies above charm thresholds outside the resonances (5.0 and 5.2 GeV) and below charm threshold (3.6 GeV), *viz.*;

$$\frac{s}{\beta} \frac{d\sigma^{charm}}{dx} (\pi^\pm) = \frac{s}{\beta} \frac{d\sigma}{dx} (\pi^\pm, \sqrt{s} = 5 \text{ GeV}) - \frac{s}{\beta} \frac{d\sigma}{dx} (\pi^\pm, \sqrt{s} = 3.6 \text{ GeV}) .$$

The charm contributions determined in this manner are plotted in figs. 18a, b. Within errors the same result is found whether the 5.0 or 5.2 GeV data are used to define the post-charm threshold data. For comparison the precharm scaling cross sections measured at 3.6 GeV are also shown. In the pion case the charm contribution is large for small x ($x \lesssim 0.2$) and exceeds the 3.6 GeV values. It falls off rapidly towards higher x values. The descent is steeper than for the precharm data. For x values above 0.3 the charm contribution is close to zero. The data for kaon production behave in a similar manner although the conclusions are less firm because of the larger statistical errors. For x values between 0.3 and 0.4 the charm contribution is larger than the 3.6 GeV data. For x values above 0.4 the charm contribution is small.

Along the same lines we have determined the average number of charged pions, kaons and nucleons produced per charm event, e.g.,

$$\langle n_{\pi^\pm}^{charm} \rangle = \frac{\int \frac{d\sigma}{dp} (\pi^\pm, \sqrt{s} = 5 \text{ GeV}) \, dp - \int \frac{d\sigma}{dp} (\pi^\pm, \sqrt{s} = 3.6 \text{ GeV}) \, dp}{\sigma_{tot}(5 \text{ GeV}) - \sigma_{tot}(3.6 \text{ GeV})} .$$

The resulting multiplicities in fig. 14 are compared to those obtained by averaging over all events [*]. It is interesting to note that within errors the final state shows the

---

[*] Note that no distinction is made between directly produced particles and those coming, e.g., from a weak decay of D or F mesons.
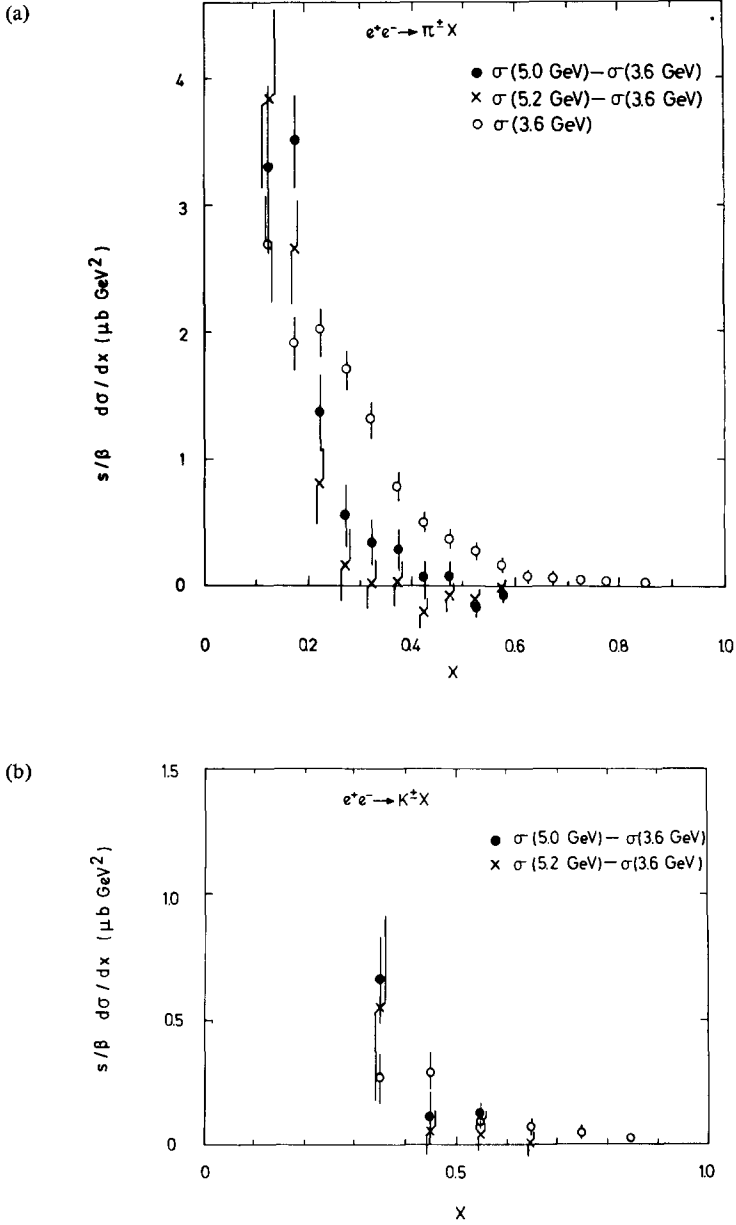
(a)

(b)

Fig. 18. (a) The charm contribution to the scaling cross section of $\pi^{\pm}$ production determined as the difference between the 3.6 GeV and 5.0 GeV data (♦), and as the difference between the 3.6 GeV and 5.2 GeV data (×). The open points (◊) show the $\pi^{\pm}$ scaling cross section measured below charm threshold at 3.6 GeV. (b) The same for $K^{\pm}$ production.

same number of $\pi^{\pm}$, and $\bar{p}$, p per charm event as for a light quark event (3.6 GeV data). However, about twice as many $K^{\pm}$ are observed in a charm event [4]. This is in qualitative accordance with the GIM mechanism [18].

5.5. Fits to the scaling cross sections

We have fitted the scaling cross sections to various functional forms suggested by theory.

(i) As noted above the scaling cross sections fall off exponentially for x values above some minimum value. Fits of the form

$$\frac{s}{\beta}\frac{d\sigma}{dx} = a \exp(-bx) \tag{5.2}$$

led to the a and b values given in table 5. The slope values lie between 8 and 9.

(ii) The cross section $(s/\beta) \, d\sigma/dx$ for small x is expected to rise proportional to x^{-1} as x approaches the lower bound $2m/\sqrt{s}$. This form leads to a multiplicity rising logarithmically with s, provided $\sigma^{tot} \sim s^{-1}$. Fig. 19 shows the distributions of the first moment, $x(s/\beta) \, d\sigma/dx$ for the three types of particles in the different energy bins. The data are consistent with $x(s/\beta) \, d\sigma/dx$ approaching a constant as $x \to 0$, i.e., $d\sigma/dx \sim x^{-1}$ for $x \to 0$. We have fitted these distributions to polynomials of the form

$$x \frac{s}{\beta}\frac{d\sigma}{dx} = \sum a_n (1-x)^n . \tag{5.3}$$

Good fits were obtained keeping all terms from $n = 1$ to 8 and for $n = 1, 2, 6, 7, 8$. The resulting coefficients a_n are tabulated in table 6. Note that the coefficients alternate in sign. The individual terms make large, positive or negative, contributions which almost cancel each other.

Table 5
Fits to the scaling cross sections for pion-production, $(s/\beta) \, d\sigma/dx = a \exp(-bx)$; the x regions used for the fits are indicated

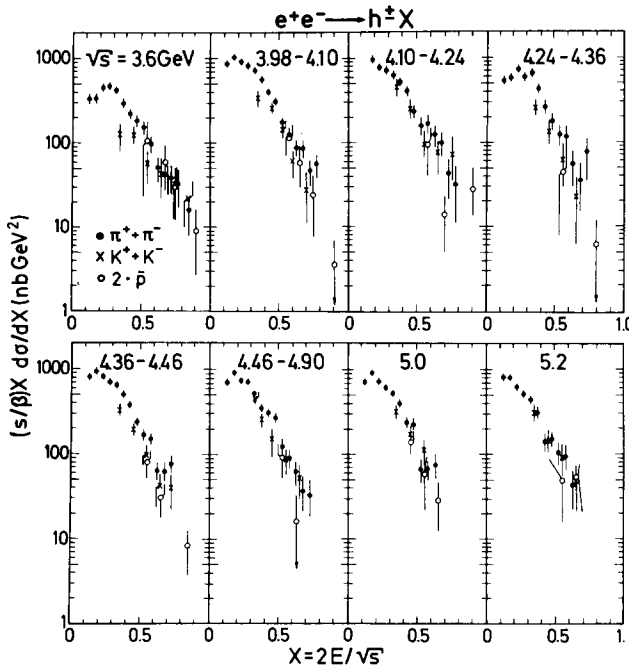| $\sqrt{s}$ (GeV)	$x_{min}-x_{max}$	a (nb · GeV^2)	b
3.60–3.67	0.3–0.9	18.2 ± 3.8	8.2 ± 0.5
3.98–4.10	0.3–0.9	28.6 ± 3.8	8.1 ± 0.3
4.10–4.24	0.2–0.8	20.8 ± 2.3	7.6 ± 0.3
4.24–4.36	0.2–0.75	23.1 ± 3.1	8.4 ± 0.4
4.36–4.46	0.2–0.75	23.4 ± 1.7	7.9 ± 0.2
4.46–4.98	0.15–0.75	24.1 ± 1.8	8.5 ± 0.2
5.0	0.15–0.65	26.9 ± 2.3	9.0 ± 0.3
5.2	0.15–0.65	22.5 ± 2.7	9.1 ± 0.4

Fig. 19. The first moment $(s/\beta)\, x\, d\sigma/dx$ of the scaling cross sections. Same data as in fig. 11.

(iii) In ref. [19] an attempt is made to describe inclusive particle spectra in terms of quark fragmentation functions. The cross section is decomposed into valence-quark and sea-quark contributions:

$$\frac{s}{\beta}\frac{d\sigma}{dx} = \sum_{q=u,d,s,c} a_v^q x^{m_v}(1-x)^{n_v} + a_s^q x^{m_s}(1-x)^{n_s} \ . \tag{5.4}$$

The powers $m_{v,s}$ and $n_{v,s}$ are fixed by certain plausibility arguments leading to

$$\frac{s}{\beta}\frac{d\sigma}{dx} = a_v \frac{1}{\sqrt{x}}(1-x) + a_s \frac{1}{x}(1-x)^2 \ . \tag{5.5}$$

We have compared this form to the pion data and found that it describes the data poorly. Therefore the powers n_v and n_s were treated as free parameters. Good fits were obtained but the error on the coefficient a_s was of the same size as a_s (see table 7) indicating that the data can be described by the first term alone. The data were then fitted to the form

$$\frac{s}{\beta}\frac{d\sigma}{dx} = a_v \frac{1}{\sqrt{x}}(1-x)^{n_v} \ , \tag{5.6}$$

treating a_v and n_v as fit parameters. The fit results are given in table 7. The power n_v is seen to rise from a value near 3 below charm threshold to $\sim$4.5 at 5 GeV.

Table 6
Fits to the first moment of the scaling cross sections for pion production, $x(s/\beta) \, d\sigma/dx = \sum_n a_n(1-x)^n$: a in $(\mu b \cdot GeV^2)$

(a) $i = 1 \dots 8$

√s (GeV)	a_1	a_2	a_3	a_4	a_5	a_6	a_7	a_8
3.60–3.67	−0.03 ± 0.01	0.18 ± 0.04	4.85 ± 0.08	−14.63 ± 0.11	0.76 ± 0.08	53.07 ± 0.11	−62.95 ± 0.14	17.43 ± 0.17
3.98–4.10	0.20 ± 0.08	−0.27 ± 0.11	0.29 ± 0.48	−0.29 ± 0.25	6.03 ± 1.31	4.80 ± 0.50	−6.75 ± 0.92	−4.96 ± 1.56
4.10–4.24	0.21 ± 0.20	−0.44 ± 0.56	1.48 ± 0.63	−0.93 ± 0.58	2.65 ± 2.44	5.96 ± 0.56	−8.60 ± 0.86	0.06 ± 2.84
4.24–4.36	0.21 ± 0.09	−0.92 ± 0.08	4.04 ± 0.76	−8.48 ± 0.35	−3.26 ± 0.96	57.75 ± 2.85	−73.03 ± 1.47	22.46 ± 3.45
4.36–4.46	0.14 ± 0.10	0.16 ± 0.31	2.56 ± 0.09	−13.31 ± 0.07	8.82 ± 0.63	54.45 ± 0.35	−80.68 ± 1.50	27.08 ± 1.81
4.46–4.98	−0.05 ± 0.08	0.97 ± 0.41	0.11 ± 0.24	−82.23 ± 0.25	2.70 ± 0.87	53.26 ± 0.14	−70.65 ± 0.45	21.08 ± 1.08
5.0	0.34 ± 0.10	−0.72 ± 0.31	2.35 ± 0.19	−11.22 ± 0.45	5.85 ± 0.15	54.80 ± 1.35	−73.76 ± 0.14	21.46 ± 1.65
5.2	0.06 ± 0.13	−0.03 ± 0.16	0.32 ± 0.35	−0.50 ± 0.50	1.76 ± 0.84	6.95 ± 0.56	−9.48 ± 1.45	1.80 ± 0.43

(b) $i = 1, 2, 6, 7, 8$

√s (GeV)	a_1	a_2	a_6	a_7	a_8
3.60–3.67	0.18 ± 0.01	−0.36 ± 0.03	38.8 ± 0.1	−75.8 ± 0.1	37.1 ± 0.1
3.98–4.10	0.12 ± 0.09	0.21 ± 0.36	13.4 ± 2.2	−4.5 ± 0.9	10.5 ± 3.4
4.10–4.24	0:24 ± 0.15	−0.35 ± 0.65	50.5 ± 33.0	−102.4 ± 77.0	54.6 ± 47.7
4.24–4.36	0.31 ± 0.10	−0.88 ± 0.33	50.4 ± 7.3	−91.0 ± 16.6	40.8 ± 10.2
4.36–4.46	0.35 ± 0.06	−0.84 ± 0.15	52.2 ± 0.5	−93.8 ± 1.2	42.4 ± 0.6
4.46–4.98	0.02 ± 0.05	0.27 ± 0.15	6.1 ± 1.7	7.3 ± 0.6	−14.8 ± 1.4
5.0	0.37 ± 0.04	−0.83 ± 0.06	12.0 ± 0.4	4.5 ± 0.1	17.9 ± 0.2
5.2	0.18 ± 0.15	−0.21 ± 0.47	4.2 ± 11.9	7.0 ± 26.4	11.2 ± 15.4

Table 7
Fits to the scaling cross section for pion production

(a) $\frac{s}{\beta}\frac{d\sigma}{dx}(e^+e^- \to \pi^\pm X) = a_v \frac{1}{\sqrt{x}}(1-x)^{n_v} + a_s \frac{1}{x}(1-x)^{n_s}$

(b) $\frac{s}{\beta}\frac{d\sigma}{dx} = a_v \frac{1}{\sqrt{x}}(1-x)^{n_v}$

$\sqrt{s}$ (GeV)	a_v (μb·GeV^2)	a_s (μb·GeV^2)	n_v	n_s	χ^2/n_f	a_v (μb·GeV^2)	n_v	χ^2/n_f
3.60–3.67	2.8 ± 0.6	−1.2 ± 0.5	3.5 ± 0.3	10 ± 4	1.4	1.83 ± 0.13	2.9 ± 0.1	2.3
3.98–4.10	5.1 ± 0.2		3.8 ± 0.1		2.0	4.93 ± 0.23	3.7 ± 0.1	2.1
4.10–4.24	4.7 ± 0.5	0.05 ± 0.10	4.1 ± 0.4	0.4 ± 1.3	0.8	4.48 ± 0.36	3.7 ± 0.1	0.8
4.24–4.36	5.4 ± 1.4	−2.6 ± 1.1	4.4 ± 0.4	11.2 ± 4.6	1.7	3.05 ± 0.22	3.5 ± 0.2	2.9
4.36–4.46	5.3 ± 0.6	−3.3 ± 2.4	4.0 ± 0.2	16.2 ± 6.4	1.7	4.02 ± 0.16	3.6 ± 0.1	4.0
4.46–4.90	5.3 ± 0.5	−4.8 ± 4.5	4.4 ± 0.2	21 ± 7	1.2	4.26 ± 0.23	4.0 ± 0.1	2.1
5.0	6.5 ± 1.2	−4.6 ± 6.0	5.1 ± 0.4	18 ± 12	1.5	4.74 ± 0.28	4.4 ± 0.2	3.0
5.2	4.8 ± 0.6	−8.6 ± 10	4.9 ± 0.3	37 ± 40	1.1	4.56 ± 0.38	4.8 ± 0.3	0.8

6. Comparison with other experiments

We first compare our data with experiments that did not separate the contributions from different type of charged particles. Since the particle mass is not known in these experiments, instead of the scaling variable $x = 2E/\sqrt{s}$, the fractional momentum $x_p = 2p/\sqrt{s}$ is used. In fig. 20 we compare our results on $s \, d\sigma/dx$ summed over $\pi^\pm$, $K^\pm$ and $2 \cdot \bar{p}$ with those from SLAC-LBL [14] and from PLUTO [20]. For x values up to 0.6 the three experiments agree within their systematic uncertainties; at higher x values a discrepancy between SLAC-LBL and PLUTO data is observed.

The Maryland-Princeton-Pennsylvania collaboration has published [21] cross-section data on $\pi^\pm$ and $K^\pm$ production at $\sqrt{s} = 4.8$ GeV. They are shown in fig. 21 together with our results obtained at $\sqrt{s} = 5$ GeV. The agreement between the two experiments is good.
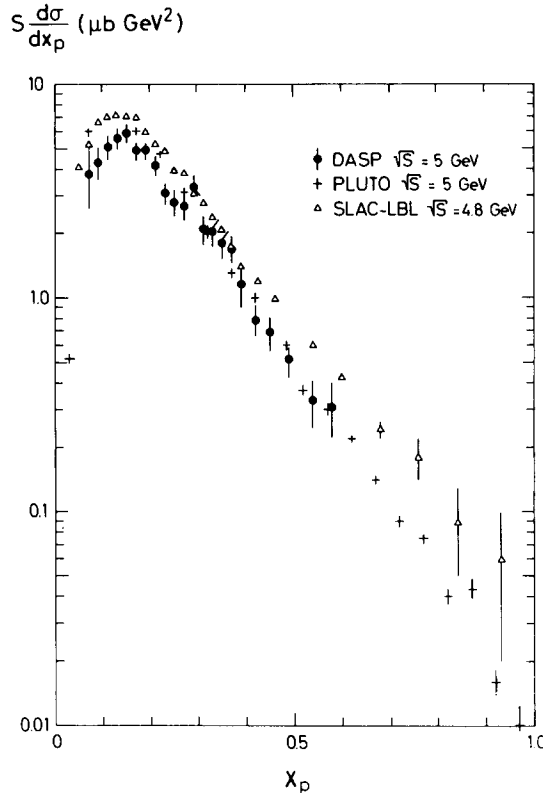
$$s \frac{d\sigma}{dx_p} \; (\mu b \; GeV^2)$$

Fig. 20. The quantity $s \, d\sigma/dx_p$, *versus* $x_p = 2p/\sqrt{s}$ summed over all charged hadrons as measured in this experiment (♦), by SLAC-LBL (⋏), ref. [14], and PLUTO (+), ref. [20].

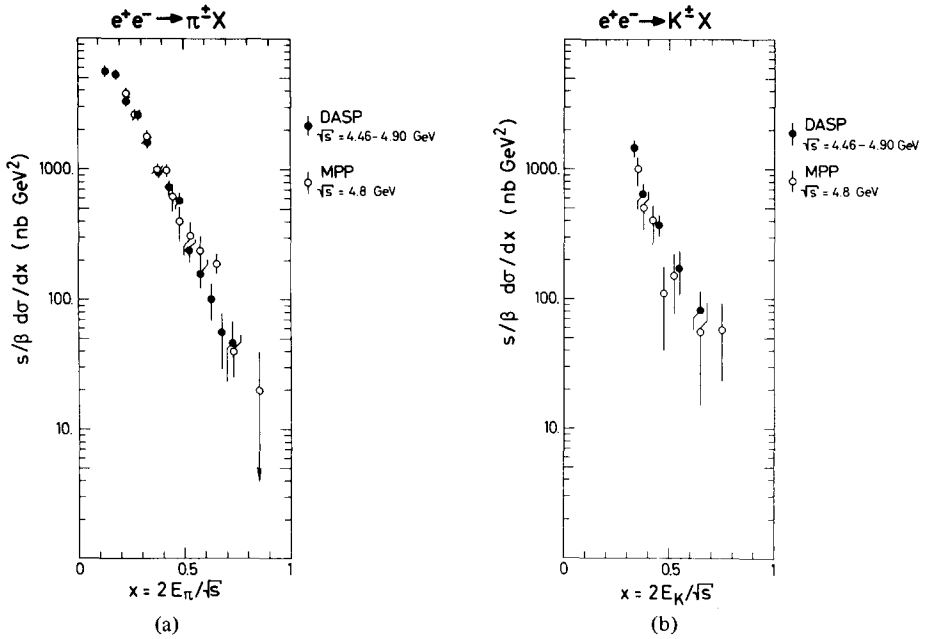Fig. 21 (a) The scaling cross section $(s/\beta)\, d\sigma/dx$ for $\pi^{\pm}$ as measured in this experiment (♦) and by Maryland-Princeton-Pavia (♢), ref. [21]. (b) The same for $K^{\pm}$ production.

7. e^+e^- annihilation and inelastic sp scattering

Inclusive antiproton production by e^+e^- annihilation,

$$e^+e^- \to \bar{p}X \tag{7.1}$$

and electron-proton scattering,

$$ep \to eX \tag{7.2}$$

are related by crossing. If scaling holds, the structure functions for one process can be calculated from those of the other one for the elastic case, $x = \omega = 1$, where $\omega = 2p \cdot q/(-q^2)$ is the scaling variable for electron-nucleon scattering. More precisely one has

$$e^+e^- \to \bar{p}X: \qquad \bar{F}_1(x = 1) = -F_1(\omega = 1)\,,$$

$$ep \to eX: \qquad \bar{F}_2(x = 1) = -F_2(\omega = 1)\,, \tag{7.3}$$

with $F_i(x)$ and $\bar{F}_i(x)$ defined as the structure functions in the scaling limit (e.g., $\bar{F}_1(x) = -m\bar{W}_1(x))$ [15].

An analytical continuation which would connect points in the inelastic region

($x < 1$ and $\omega > 1$) is in general not possible [22]. However, Gribov and Lipatov [23] studying both processes in a field theoretic model predicted the following relations:

$$F_1\left(\omega = \frac{1}{x}\right) = -x\overline{F}_1(x) ,$$

$$F_2\left(\omega = \frac{1}{x}\right) = -x^3\overline{F}_2(x) . \qquad (7.4)$$

The cross section for antiproton production reads then

$$\frac{x}{\sigma_{\mu\mu}} \frac{\mathrm{d}\sigma}{\mathrm{d}x}(e^+e^- \to \overline{p}X) = 3\beta\left\{xF_1\left(\omega = \frac{1}{x}\right) - \frac{1}{6}\beta^2 F_2\left(\omega = \frac{1}{x}\right)\right\} , \qquad (7.5)$$

where $\sigma_{\mu\mu}$ is the muon pair-production cross section, $\sigma_{\mu\mu} = 4\pi\alpha^2/3s$. Note that the first term in eq. (7.5) is the dominant one.

Fig. 22 shows the ratio $R_{p+\overline{p}} = 2\sigma(\overline{p})/\sigma_{\mu\mu}$ of p and $\overline{p}$ production to the μ pair cross section as a function of c.m. energy. The full points represent the cross section for $\overline{p}$ momenta above 0.5 GeV/c. The open points show the cross section integrated over all momenta. They were obtained by extrapolating $(E/4\pi p^2)\,\mathrm{d}\sigma/\mathrm{d}p\,(E)$ towards $p = 0$ with an exponential.

Fig. 23 shows $(x/\sigma_{\mu\mu})\,\mathrm{d}\sigma/\mathrm{d}x$ averaged over the c.m. energy region from 3.6 to 4.5 GeV which is below the charm baryon threshold. The Gribov-Lipatov prediction (see curve in fig. 23) was computed from the values of the structure functions measured by ref. [24] imposing the same acceptance criteria as for the data; first the cross section was calculated from (4.2) and (7.4) in the accepted $\cos\theta$ range; then
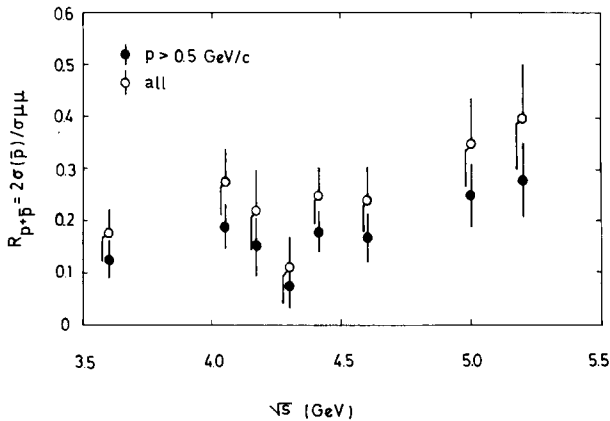

Fig. 22. The ratio $R_{p+\overline{p}} = 2\sigma(\overline{p})/\sigma_{\mu\mu}$ for p and $\overline{p}$ production to the μ pair cross section. Full points: $\overline{p}$ momenta above 0.5 GeV/c. Open points: all momenta.
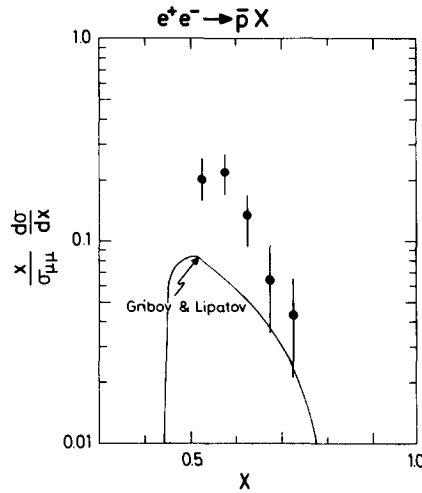
Fig. 23. The quantity $(x/\sigma_{\mu\mu})\,\mathrm{d}\sigma/\mathrm{d}x$ *versus* x for $e^+e^- \to \bar{p}X$ averaged over c.m. energies from 4.0 to 5.2 GeV. The curve shows the prediction of Gribov and Lipatov (ref. [23]).

the cross section was extrapolated to $\cos\theta = \pm 1$ assuming isotropy. Since scale invariance is not exactly satisfied by inelastic electron-proton scattering $F_1(\omega)$, $F_2(\omega)$ or rather $mW_1(q^2, s)$ and $\nu W_2(q^2, s)$ were taken at $-q^2 = s$.

The Gribov-Lipatov prediction fails to describe the data taken quantitatively. The theoretical curve is always below the measured points. The discrepancy appears to increase towards smaller values of x reaching a factor of three at $x = 0.5$. Part of this failure, if not all, may have to be attributed to contributions of the type

$$e^+e^- \to h^*X \,\mathrm{m} \qquad h^* = \overline{\Lambda} \quad , \qquad \overline{\Sigma} \quad , \qquad \overline{N}^* \quad , \qquad \text{etc.}\,,$$
$$\qquad\qquad\qquad \hookrightarrow \bar{p}\,... \qquad \hookrightarrow \bar{p}\,... \qquad \hookrightarrow \bar{p}\,...$$

which should be excluded from the e^+e^- data before a comparison is made [25].

8. Comparison with inclusive spectra from J/ψ decay

As mentioned before, annihilation into hadrons at high energies appears to proceed *via* a primary quark-antiquark pair. The direct hadronic decay of the J/ψ on the other hand is believed to have three gluons as an intermediate state. For this reason one might expect the J/ψ to yield a steeper falling x spectrum (i.e., more low-momentum particles) as compared to non-resonant hadron production. In fig. 24 the quantity

$$\frac{1}{\sigma_{tot}}\frac{1}{\beta}\frac{\mathrm{d}\sigma}{\mathrm{d}x}$$

is shown at a c.m. energy of 3.6 GeV (below charm threshold) for charged pions,
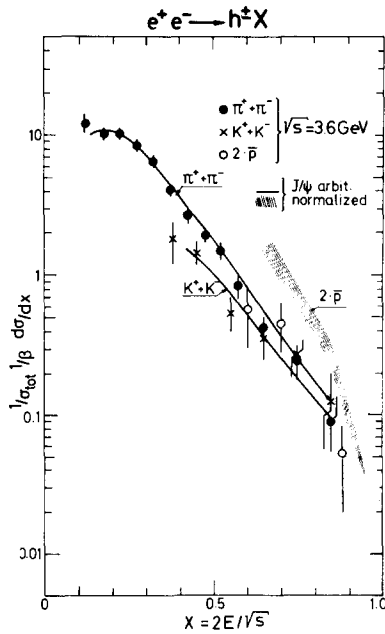
Fig. 24. The quantities $1/(\sigma_{tot}\beta) \, d\sigma/dx$ *versus* x for the sum of $\pi^+ + \pi^-$, $K^+ + K^-$ and twice the $\bar{p}$ production at 3.6 GeV and from J/ψ decay. The J/ψ cross sections are shown by the curves and the hatched band. They have been scaled by a common normalization factor.
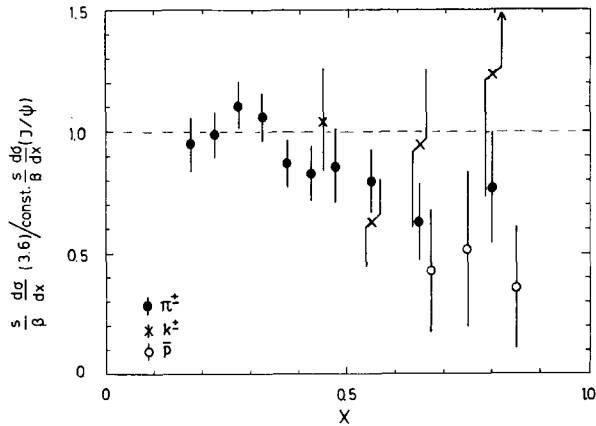

Fig. 25. The ratio of the scaling cross sections $(s/\beta) \, d\sigma/dx$ from 3.6 GeV over those from J/ψ decay for $\pi^{\pm}$, $K^{\pm}$ and $2 \cdot \bar{p}$ production. The J/ψ data have been multiplied by a common factor so as to have the same value for the integral $\int (s/\beta)(d\sigma/dx) \, dx$ for $\pi^{\pm}$ production.

kaons and twice the $\bar{p}$ yield. Curves are shown to represent the J/ψ data normalized by a common factor to make the integrated pion cross sections agree. Within errors no difference is observed in the shape of the pion cross sections and the kaon cross sections measured at the two energies. This can also be seen from fig. 25 where the ratio of the scaling cross sections has been plotted as a function of x. Actually the J/ψ data tend to have slightly more high-energy pions. Most likely the energy of ~3 GeV is too low for the two mechanisms to produce noticeably different spectra. The only difference occurs in the antiproton to pion ratio which is a factor of two to three larger for the J/ψ decay than at 3.6 GeV.

9. Summary

We have measured inclusive production of $\pi^{\pm}$, $K^{\pm}$ and $\bar{p}$ by $e^{+}e^{-}$ annihilation in the energy region around the charm threshold ($\sqrt{s}$ = 3.6–5.2 GeV). The pion and kaon yields are found to increase by a factor of two to three when crossing the charm threshold. Above charm threshold on the average 3–4 $\pi^{\pm}$, 0.5–0.6 $K^{\pm}$ and 0.05–0.08 p, $\bar{p}$ are produced per event. While the magnitude and shape of the momentum spectra of the three particle species is quite different, the invariant cross sections $(E/4\pi p^2)$ $d\sigma/dp$ plotted as a function of particle energy fall on the same curve to within 20 or 30% accuracy. A similar agreement is observed for the scaling cross sections (s/β) $d\sigma/dx$, which to a good approximation are proportional to $xm\bar{W}_1(x, s)$. The scaling cross sections measured for $\pi^{\pm}$ below charm threshold ($\sqrt{s}$ = 3.6 GeV) and above charm threshold and the resonance region ($\sqrt{s}$ = 5.2 GeV) have been compared to each other. For $x < 0.25$ the cross section rises by a factor of 2.5 to 2 between $\sqrt{s}$ = 3.6 and $\sqrt{s}$ = 5.2 GeV. At $x > 0.3$ the two cross-section sets agree within errors.

By taking the difference between particle production below and above charm threshold we have determined the charm contribution to charged pion and kaon production. For pions the charm contribution below x = 0.2 exceeds the pion yield measured below charm threshold. Towards higher x values the charm contribution drops rapidly and is close to zero for x above 0.3. The kaon data show a similar tendency. For x values above 0.4 the charm contribution is small. Inclusive antiproton production, $e^{+}e^{-} \rightarrow \bar{p}X$, has been compared to the crossing-related inelastic electron-proton scattering, ep $\rightarrow$ eX. The Gribov-Lipatov prediction is found to fall short of the observed $\bar{p}$ yield by a factor of 2–4. This may be due to contributions from non-direct $\bar{p}$ production, e.g., *via* isobar or hyperon production and decay.

No significant difference has been found in the shape of inclusive $\pi^{\pm}$, $K^{\pm}$ or $\bar{p}$ spectra produced in J/ψ decay or at 3.6 GeV. The first process is assumed to proceed primarily *via* three-gluon decay, the latter by quark-pair formation.

and maintaining DESY, DORIS, DASP and the Computer Center. The non-DESY members of the collaboration wish to thank the DESY directorate for their hospitality. We also want to thank Drs. J. Ellis, J. Körner, G. Schierholz and T. Walsh for fruitful discussions.

References

[1] C.G. Hanson et al., Phys. Rev. Lett. 35 (1975) 1609;
C.G. Hanson, Talk given at the 13th Recontre de Moriond, 1978, SLAC-PUB-2118.
[2] PLUTO collaboration, talk given by H. Meyer at the JET Meeting in Copenhagen (July 1978).
[3] DASP collaboration, R. Brandelik et al., Phys. Lett. 67B (1977) 358.
[4] DASP collaboration, R. Brandelik et al., Phys. Lett. 67B (1977) 363.
[5] DASP collaboration, W. Braunschweig et al., Phys. Lett. 63B (1976) 115.
[6] M. Schliwa, thesis, University of Hamburg (1979).
[7] W. Braunschweig, E. König, W. Sturm and W. Wallraff, Nucl. Instr. 134 (1976) 261.
[8] K. Sauerberg, thesis, University of Hamburg (1979).
[9] DASP collaboration, R. Brandelik et al., Phys. Lett. 76B (1978) 361.
[10] R. Fries, thesis, University of Hamburg (1978).
[11] A. Jaccarini, N. Arteago-Romero, J. Parisi and P. Kessler, Compt. Rend. B269 (1969) 153, 1129;
N. Arteago-Romero, A. Jaccarini, P. Kessler and J. Parisi, Phys. Rev. D3 (1971) 1569;
S.J. Brodsky, T. Kinoshita and H. Terazawa, Phys. Rev. Lett. 25 (1970) 972.
[12] DASP collaboration, R. Brandelik et al., Phys. Lett. 70B (1977) 125, 387; 73B (1978) 109
[13] G. Bonneau and F. Martin, Nucl. Phys. B27 (1971) 381.
[14] C.G. Hanson, talk given at 18th Int. Conf. on high-energy physics, Tbilisi, USSR (1976); SLAC-PUB-1814 (1976).
[15] S.D. Drell, D. Levy and T.M. Yan, Phys. Rev. 187 (1969) 2159; D1 (1970) 1035, 1616, 2402.
[16] H.B. Thacker and J.J. Sakurai, Phys. Lett. 36B (1971) 103;
Y.S. Tsai, Phys. Rev. D4 (1971) 2821; SLAC-PUB-2105 (1978);
F.J. Gilman and D.H. Miller, Phys. Rev. D17 (1978) 1845.
[17] British-Scandinavian collaboration, B. Alper et al., Nucl. Phys. B87 (1975) 19.
[18] S.L. Glashow, J. Iliopoulos and L. Maiani, Phys. Rev. D2 (1970) 1285.
[19] S. Wada, T. Inami and S. Kitakado, University of Tokyo preprint, UT-Komaba 76-11 (1976).
[20] PLUTO collaboration, A. Bäcker, thesis, Gesamthochschule Siegen, 1977; Internal report DESY F33-77/03.
[21] T. Atwood et al., Phys. Rev. Lett. 35 (1975) 704;
H.F.W. Sadrozinski, Proc. 1977 Int. Symp. on Lepton and photon interactions at high enel gies, Hamburg, ed. F. Gutbrod (DESY, 1977) p. 47.
[22] R. Gatto, P. Menotti and I. Vendramia, Nuovo Cim. Lett. 4 (1972) 35;
E. Gatto and G. Preparata, Nucl. Phys. B47 (1972) 313.
[23] V.N. Gribov and L.N. Lipatov, Phys. Lett. 37B (1971) 78.
[24] E.M. Riordan et al., SLAC-PUB-1634 (1975).
[25] G. Schierholz and M.G. Schmidt, Nucl. Phys. B101 (1975) 429.